J. Fluid Mech. (2025), *vol.* 1018, A21, doi:10.1017/jfm.2025.10497

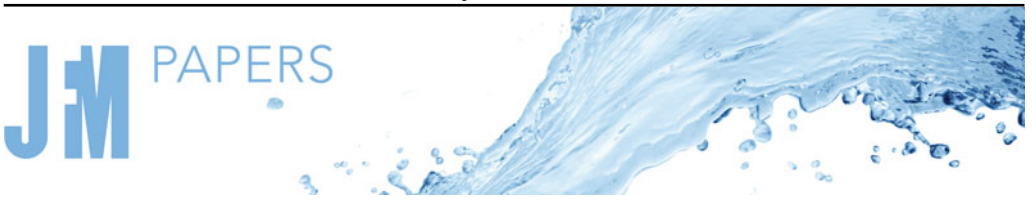

Boundary layer asymmetry in turbulent spherical Rayleigh–Bénard convection: combined dependence on Prandtl number and radius ratio

Yifeng Fu[1], **Shujaut H. Bader**[1] **and Xiaojue Zhu**[1]

[1]Max Planck Institute for Solar System Research, 37077 Göttingen, Germany

Corresponding author: Xiaojue Zhu, zhux@mps.mpg.de

(Received 19 February 2025; revised 20 May 2025; accepted 16 July 2025)

Direct numerical simulations (DNS) are performed to investigate the dependence of the Prandtl number (Pr) and radius ratio ($\eta = r_i/r_o$) on the asymmetry of the mean temperature radial profiles in turbulent Rayleigh–Bénard convection (RBC) within spherical shells. Unlike planar RBC, the temperature drop, and the thermal and viscous boundary layer thicknesses, at the inner and outer boundaries are not identical in spherical shells. These differences in the boundary layer properties in spherical RBC contribute to the observed asymmetry in the radial profiles of temperature and velocity. The asymmetry originates from the differences in curvature and gravity at the two boundaries, and in addition, is influenced by Pr. To investigate the η and Pr dependence of these asymmetries, we perform simulations of Oberbeck–Boussinesq convection for $\eta = 0.2$, 0.6 and $0.1 \leqslant Pr \leqslant 50$, and for a range of Rayleigh numbers (Ra) varying between 5×10^6 and 5×10^7. The Prandtl numbers that we choose cover a broad range of geophysical relevance, from low-Pr regimes ($Pr = 0.1$) representative of gas giants such as Jupiter and Saturn, to high-Pr regimes characteristic of organic flows used in the convection experiments ($Pr = 50$). A centrally condensed mass, with the gravity profile $g \sim 1/r^2$, is employed in this study. Our results show that the asymmetry at smaller η exhibits a stronger Pr dependence than at larger η. Various assumptions for quantifying this asymmetry are evaluated, revealing that different assumptions are valid in different Pr regimes. It is shown that the assumption of the equal characteristic plume separation at the inner and outer boundaries, as well as the assumption of the identical thermal fluctuation scales between the two boundary layers, is valid only for $0.2 \lesssim Pr \lesssim 1$. In contrast, assumptions based on the equivalency of the local thermal boundary layer Rayleigh numbers and laminar natural-convective boundary layers are validated at $Pr = 50$ for the explored parameter space. Furthermore, new assumptions based on the statistical analysis of the inter-plume islands are proposed for $Pr = 0.1$ and 50, and these are validated against the DNS data. These findings provide insights into the

(Pr, η) dependence of asymmetry in spherical RBC, and offer a framework for studying similar systems in geophysical and astrophysical contexts.

Key words: turbulence simulation, Bénard convection, plumes/thermals

1. Introduction

Thermal convection in spherical shells is of vital importance in geophysical and astrophysical systems, including Earth's mantle convection (Davies & Richards 1992), planetary interiors (Aurnou *et al.* 2008; Wicht & Sanchez 2019), and stellar convection zones (Hanasoge, Gizon & Sreenivasan 2016). Compared to Rayleigh–Bénard convection (RBC) in planar geometries, spherical RBC exhibits two key differences in convection dynamics: (i) the scaling relationships between the system response parameters – such as the dimensionless heat transfer (Nusselt number, Nu) and dimensionless momentum transfer (Reynolds number, Re) – and the input parameters (Rayleigh number, Ra, and Prandtl number, Pr) differ from those observed in planar RBC; (ii) the differences in the radius of curvature at the inner and outer boundaries, and the radially varying gravity, lead to the asymmetric thermal and velocity boundary layers (Gastine, Wicht & Aurnou 2015; Fu *et al.* 2024). This asymmetry is also influenced by Pr (Tilgner 1996). To accurately model the heat and momentum transport in spherical convection, it is imperative to gain an understanding of the asymmetry, and its dependence on η and Pr. In this work, we make an effort in this direction.

Experimental and numerical studies have provided significant insights into the dynamics of convection in spherical shells. Experimental studies, such as the 'GeoFlow' experiments on the International Space Station (ISS) (Egbers *et al.* 2003; Futterer *et al.* 2010; Zaussinger *et al.* 2020), use electrically induced radial body forces to mimic gravity, and focus mainly on mantle convection with high Pr ($40 < Pr < 200$). However, these experiments are limited to relatively low Rayleigh numbers ($Ra < 10^7$) due to the constraints on the electric field strength and fluid properties. Numerical studies, on the other hand, have explored a broader parameter space. For example, Tilgner (1996) investigated the scaling of global heat and momentum transport in spherical RBC, examining $Nu(Ra, Pr)$ and $Re(Ra, Pr)$ relations in the ranges $0.06 \leqslant Pr \leqslant 10$ and $4 \times 10^3 \leqslant Ra \leqslant 8 \times 10^5$ at a fixed radius ratio $\eta = 0.4$ with a linear gravity profile ($g(r) \sim r$). The author reports that the scalings $Nu \sim Ra^{0.24}$ and $Re \sim Ra^{0.5}$ are valid within the explored parameter space. Similarly, Gastine *et al.* (2015) performed direct numerical simulations (DNS) to study spherical RBC with various gravity profiles ($g(r) \in \{r/r_o, 1, (r_o/r)^2, (r_o/r)^5\}$) and radius ratios ($0.2 \leqslant \eta \leqslant 0.95$) at $Pr = 1$. The scaling behaviours of $Nu(Ra)$ and $Re(Ra)$ were studied exclusively for the simulations with $Ra \leqslant 10^9$ and at a specific radius ratio $\eta = 0.6$. Recently, Fu *et al.* (2024) systematically investigated the η dependence of $Nu(Ra)$ and $Re(Ra)$ scalings for $0.2 \leqslant \eta \leqslant 0.8$ at $Pr = 1$. They observed larger scaling exponents for smaller η cases, suggesting that the simulations with smaller η reach the classical $Nu \sim Ra^{1/3}$ regime at a relatively lower Ra. The η dependence in $Nu(Ra)$ scaling relations was also quantified. These results highlight the impact of geometric curvature on the global transport properties in spherical RBC.

Boundary layer asymmetry studies in spherical RBC have primarily focused on two specific Pr regimes: $Pr = 1$, and the asymptotic $Pr \to \infty$ limit. The asymmetry of thermal boundary layers in spherical RBC is typically characterised by the two key parameters: the mid-layer bulk temperature ϑ_{mid}, and the thermal boundary layer thickness ratio $\lambda_\vartheta^i/\lambda_\vartheta^o$,

where λ_ϑ^i and λ_ϑ^o represent the thicknesses of the inner and outer thermal boundary layers, respectively.

For mantle convection at $Pr \to \infty$, Jarvis (1993) proposed that the thermal boundary layers are equally stable, leading to equal thermal boundary layer Rayleigh numbers at both the boundaries, where the thermal boundary layer Rayleigh number is defined based on the thermal boundary layer thickness as the length scale, and the temperature drop across the thermal boundary layer as the temperature scale. This assumption was extended by Vangelov & Jarvis (1994) and Jarvis, Glatzmaierand & Vangelov (1995) to study the η dependence of boundary layer asymmetry in spherical RBC, which was further validated through their numerical simulations. Moreover, Shahnas *et al.* (2008) and Deschamps, Tackley & Nakagawa (2010) extended these models to systems with internal heating, highlighting the additional complexities introduced by internal heat sources.

For $Pr = 1$, Gastine *et al.* (2015) assumed equivalent mean plume separation at the edges of the inner and outer thermal boundary layers, and derived thermal boundary layer asymmetry as a function of η, validating their predictions with DNS results. They also examined the assumption proposed by Vangelov & Jarvis (1994), and found that it did not align with their DNS data at $Pr = 1$. Furthermore, they tested the assumption of the equivalency of the temperature fluctuation scales at both boundary layers (Wu & Libchaber 1991), and observed that it fits DNS data only for a gravity profile $g(r) \sim 1/r^2$ at $Pr = 1$.

Despite these efforts, existing models have been validated only at specific Pr values, either $Pr = 1$ or $Pr \to \infty$. Whether these models remain applicable to intermediate Pr regimes or require modifications remains an open question. This knowledge gap motivates the present study, which systematically investigates the Pr and η dependence of thermal boundary layer asymmetry across a broader parameter space.

In astrophysical and geophysical contexts, Pr exhibits significant variations due to differences in the material properties of the flowing medium. For example, in the Earth's outer core, Pr is estimated to lie between values 0.1 and 1 (Wicht & Sanchez 2019), while in the convective molecular layers of Jupiter and Saturn, the typical values are $Pr \approx 0.1$ (Yadav, Heimpel & Bloxham 2020). The Earth's near-surface atmosphere has Prandtl number approximately 0.7, whereas seawater has $Pr \approx 7$ (at 20 °C) and $Pr \approx 13$ (at 0 °C). Light organic liquids span a broader range, with $5 \leqslant Pr \leqslant 50$ (Shah & London 1978). Silicone oil with $Pr \approx 64.64$ was used in the GeoFlow experiment aboard the ISS to study mantle-like convection in a spherical shell geometry (Futterer *et al.* 2010). In addition to a broad range of Pr values, the radius ratio ($\eta = r_i/r_o$), which characterises the geometric configuration of spherical shells, also varies significantly among planetary bodies. Table 1 summarises the radius ratios and Prandtl numbers of selected planetary interiors. Since the asymmetry of the thermal boundary layers depends strongly on both Pr and η, understanding how this asymmetry evolves with these parameters is essential for characterising the dynamics of planetary convection. Despite its significance, the combined dependence of thermal boundary layer asymmetry on η and Pr regimes has not been investigated systematically, leaving ample room for further research.

This study investigates the dependence of thermal boundary layer asymmetry on Pr and η through DNS. The simulations consider radius ratios $\eta = 0.2$ and 0.6, spanning $0.1 \leqslant Pr \leqslant 50$ and $Ra \leqslant 5 \times 10^7$. Given the ranges of Pr and η observed in natural systems, as discussed earlier, the chosen parameter space provides a reasonable representation of diverse convection scenarios. We assess the validity of the existing models, and propose new assumptions based on the statistical analysis of the inter-plume

Planet	η	Pr	References
Earth's mantle	0.55	$\sim 10^{25}$	Shahnas *et al.* (2008), Schubert *et al.* (2001)
Earth's outer core	0.35	$0.1-1$	Christensen & Aubert (2006), Wicht & Sanchez (2019)
Jupiter	0.55–0.75	~ 0.1	Guillot *et al.* (2004), Yadav *et al.* (2020)
Saturn	0.45–0.55	~ 0.1	Christensen & Wicht (2008), Vazan *et al.* (2016), Yadav *et al.* (2020)

Table 1. Radius ratios for the selected planetary interiors in the solar system. The radius ratios for Jupiter (Guillot *et al.* 2004) and Saturn (Christensen & Wicht 2008; Vazan *et al.* 2016) are chosen as the ratio between the radii of the inner metallic-core boundary and the outer upper atmosphere boundary.

islands at the edges of the thermal boundary layers to explain the combined dependence of thermal boundary layer asymmetry on Pr and η. Specifically, we develop new models for $Pr = 0.1$ and 50, and validate them using our simulation data.

The remainder of this paper is organised as follows. Section 2 describes the governing equations, diagnostic parameters and numerical methods used in this study. Section 3 gives an overview of the boundary layer asymmetry for different η and Pr regimes. In § 4, we evaluate several existing models for quantifying thermal boundary layer asymmetry over $0.1 \leqslant Pr \leqslant 50$, identifying their respective validation ranges. Section 5 introduces new thermal boundary layer asymmetry models for $Pr = 0.1$ and 50, developed through statistical analysis of the inter-plume islands near the inner and outer boundary layer edges. This section also explores the dependence of the inter-plume island statistics on Pr and η. Finally, § 6 summarises our findings and discusses future research directions.

2. Model description

2.1. *Governing equations*

We study Oberbeck–Boussinesq convection in spherical shells with inner radius r_i and outer radius r_o. A no-slip boundary condition is employed at both boundaries for the velocity field. The temperature boundary condition is isothermal, with the inner boundary at T_i, and the outer boundary at T_o. The governing equations are non-dimensionalised by the temperature scale $\Delta T = T_i - T_o$, the length scale $d = r_o - r_i$, the viscous dissipation time scale d^2/ν, the momentum diffusive velocity scale ν/d, and the pressure scale $\rho\nu^2/d^2$. Gravity is non-dimensionalised by its value at the outer boundary $g_o = g(r_o)$. The dimensionless governing equations read

$$\boldsymbol{\nabla} \cdot \boldsymbol{u} = 0, \tag{2.1}$$

$$\frac{\partial \boldsymbol{u}}{\partial t} + \boldsymbol{u} \cdot \boldsymbol{\nabla} \boldsymbol{u} = -\boldsymbol{\nabla} p + \frac{Ra}{Pr} g T \boldsymbol{e}_r + \nabla^2 \boldsymbol{u}, \tag{2.2}$$

$$\frac{\partial T}{\partial t} + \boldsymbol{u} \cdot \boldsymbol{\nabla} T = \frac{1}{Pr} \nabla^2 T. \tag{2.3}$$

In the above equations, $\boldsymbol{u}, T, p$ represent the velocity, temperature and pressure, respectively. The equations are controlled by three input parameters,

$$Ra = \frac{\alpha g_o \, \Delta T \, d^3}{\nu \kappa}, \quad Pr = \frac{\nu}{\kappa}, \quad \eta = \frac{r_i}{r_o}, \tag{2.4}$$

where α is the thermal expansion coefficient, and ν and κ are the kinematic viscosity and thermal diffusivity, respectively. In our simulations, we assume a centrally condensed mass, with gravity profile $g(r) = (r_o/r)^2$ (Chandrasekhar 1981). A schematic of the computational domain and the coordinate system is provided in Appendix A.

2.2. *Response parameters*

We use the following notations throughout the paper for different averaging procedures. An overbar $(\bar{\cdot})$ represents the time average of a dimensionless variable f, while $\langle\cdot\rangle_s$ and $\langle\cdot\rangle$ represent the horizontal and volume averages, respectively. The definitions of these averaging procedures are

$$\overline{f} = \frac{1}{\tau}\int_{t_0}^{t_0+\tau} f\,\mathrm{d}t, \tag{2.5}$$

$$\langle f\rangle_s = \frac{1}{4\pi}\int_0^{\pi}\int_0^{2\pi} f\,\sin\theta\mathrm{d}\theta\mathrm{d}\phi, \tag{2.6}$$

$$\langle f\rangle = \frac{1}{V}\int_{r_i}^{r_o}\int_0^{\pi}\int_0^{2\pi} f\,\sin\theta r^2\mathrm{d}r\mathrm{d}\theta\mathrm{d}\phi. \tag{2.7}$$

In the above equations, θ is co-latitude and ϕ is longitude, and $V = 4\pi(r_o^3 - r_i^3)/3$ is the volume of the spherical shell.

There are two key response parameters in RBC: the Nusselt number (Nu), which represents the dimensionless heat flux, and the Reynolds number (Re), which is a dimensionless measure of flow velocity.

In Oberbeck–Boussinesq approximation, Nu for isothermal boundaries in spherical RBC reads

$$Nu = \frac{\overline{\langle u_r T\rangle_s} - \dfrac{1}{Pr}\dfrac{\mathrm{d}\vartheta}{\mathrm{d}r}}{-\dfrac{1}{Pr}\dfrac{\mathrm{d}T_c}{\mathrm{d}r}} = -\eta\left.\frac{\mathrm{d}\vartheta}{\mathrm{d}r}\right|_{r=r_i} = -\frac{1}{\eta}\left.\frac{\mathrm{d}\vartheta}{\mathrm{d}r}\right|_{r=r_o}, \tag{2.8}$$

where

$$T_c(r) = \frac{\eta}{(1-\eta)^2}\frac{1}{r} - \frac{\eta}{1-\eta} \tag{2.9}$$

is the conductive temperature profile.

The Reynolds number is defined as

$$Re = \overline{\sqrt{\langle u^2\rangle}} = \overline{\sqrt{\langle u_r^2 + u_\theta^2 + u_\phi^2\rangle}}. \tag{2.10}$$

By adopting the notations (2.5) and (2.6), the time and horizontally averaged radial profiles of the mean temperature and the mean horizontal velocity are given, respectively, by

$$\vartheta(r) = \overline{\langle T\rangle_s}, \quad Re_h(r) = \overline{\sqrt{\langle u_\theta^2 + u_\phi^2\rangle_s}}. \tag{2.11}$$

2.3. *Numerical settings and parameter space*

In this work, all the simulations are conducted by using MagIC (https://magic-sph.github.io/), which is a pseudo-spectral solver in which all the unknown variables are expanded into complete sets of functions in the radial and horizontal directions. Chebyshev

polynomials are applied in the radial direction, while spherical harmonic functions are used in the azimuthal and latitudinal directions. The equations are time-stepped by advancing the nonlinear terms using an explicit second-order Adams–Bashforth scheme, while the linear terms are time-advanced using an implicit Crank–Nicolson algorithm. At each time step, the linear terms are calculated in the spectral space, while the nonlinear terms are calculated in the physical space. For more information about MagIC, the interested reader is referred to Wicht (2002), Christensen & Wicht (2007) and Lago *et al.* (2021).

For $g(r) = (r_o/r)^2$, if we dot (2.2) with $\boldsymbol{u}$, and (2.3) with T, and average the results temporally and volumetrically, then the following exact relations can be derived (Gastine *et al.* 2015):

$$\epsilon_u = \frac{3}{1+\eta+\eta^2}\frac{Ra}{Pr^2}(Nu-1), \tag{2.12}$$

$$\epsilon_\vartheta = \frac{3\eta}{1+\eta+\eta^2}\,Nu. \tag{2.13}$$

Here, ϵ_u and ϵ_ϑ represent the time- and volume-averaged kinetic energy dissipation rate and thermal dissipation rate, respectively. Following our non-dimensionalisation, ϵ_u and ϵ_ϑ are calculated as

$$\epsilon_u = \overline{\left\langle \left(\frac{\partial u_i}{\partial x_j}\right)^2 \right\rangle}, \quad \epsilon_\vartheta = \overline{\left\langle \left(\frac{\partial T}{\partial x_i}\right)^2 \right\rangle}. \tag{2.14}$$

The Nusselt number is computed based on the gradient of temperature at the boundaries as well as the dissipation rates:

$$\left.\begin{aligned} Nu_{\epsilon_u} &= \frac{1+\eta+\eta^2}{3}\frac{Pr^2}{Ra}\epsilon_u + 1, \quad Nu_{\epsilon_\vartheta} = \frac{1+\eta+\eta^2}{3\eta}\epsilon_\vartheta, \\ Nu_b &= -\eta\frac{\mathrm{d}\vartheta}{\mathrm{d}r}\bigg|_{r=r_i}, \quad Nu_t = -\frac{1}{\eta}\frac{\mathrm{d}\vartheta}{\mathrm{d}r}\bigg|_{r=r_o}, \end{aligned}\right\} \tag{2.15}$$

where Nu_b and Nu_t follow from the definition of Nu (see (2.8)). The relative error between these Nu values is used as a measure of resolution in our simulations. A simulation is considered converged when the relative difference between these independent Nusselt number values is consistently $\lesssim 1\,\%$. Additionally, we also ensured convergence by examining the balance of the kinetic energy budget, which is the balance between the volume-averaged input buoyancy power and the volume-averaged kinetic energy dissipation rate. See Appendix A.

In addition, to validate the numerical accuracy of MagIC, we conducted two benchmark simulations using the open-source spectral code Dedalus (https://dedalus-project.org/). In the first case ($Pr = 1$, $\eta = 0.6$, $Ra = 10^6$), MagIC produced $Nu = 8.94$ and $Re = 260.46$, while Dedalus gave $Nu = 8.92$ and $Re = 260.36$. In the second case ($Pr = 10$, $\eta = 0.6$, $Ra = 10^6$), MagIC yielded $Nu = 9.17$ and $Re = 34.49$, compared to $Nu = 9.05$ and $Re = 34.14$ from Dedalus. These results show excellent agreement between the two codes, further confirming the reliability of MagIC for the problem considered in this study.

We conduct seven sets of simulations at $Pr = 0.1, 0.2, 0.5, 1, 5, 10, 50$ with $5\times10^6 \leqslant Ra \leqslant 5\times10^7$, and $\eta = 0.2$ and 0.6. For more details about the simulation parameters and grid resolution, refer to Table 3 in Appendix A.

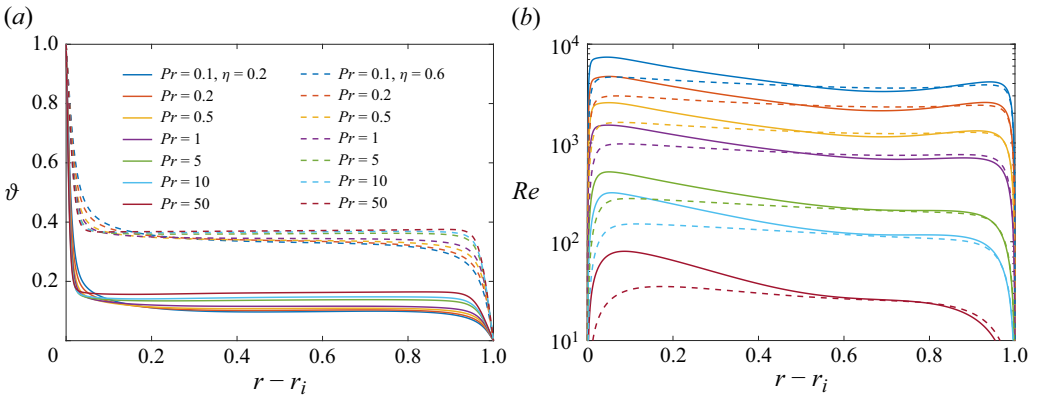

Figure 1. Radial profiles of (*a*) temperature $\vartheta(r)$, and (*b*) velocity $Re(r)$, at different η and Pr. Here, $Ra = 10^7$ for all the cases shown.

3. Velocity and temperature asymmetry

Spherical shell RBC exhibits notable differences from its planar counterpart, primarily due to the curvature of the bounding surfaces, and the radial variation of gravity. This results in asymmetry in the radial profiles of temperature and velocity fluctuations.

Figure 1 shows the time and horizontally averaged radial profiles of temperature and velocity at $Ra = 10^7$, $\eta = 0.2, 0.6$, at different Pr. As shown in figure 1(*a*), the majority of the temperature drop occurs near the boundaries. This behaviour can be attributed to the thermal shortcut (Ahlers, Grossmann & Lohse 2009) in the bulk flow. In turbulent RBC, temperature is well mixed in the bulk region, leading to a minimal temperature drop within the bulk, facilitating the majority of the temperature drop to occur within the thermal boundary layers. The mean temperature drop near the inner boundary is larger than that near the outer boundary, consistent with the observations reported by Gastine *et al.* (2015) and Fu *et al.* (2024). This phenomenon arises due to the conservation of heat flux, as well as the smaller surface area of the inner boundary compared to the outer boundary. Additionally, larger differences in curvature and gravity between the inner and outer boundaries yield larger deviations of the bulk temperature $\vartheta_{mid} = \vartheta((r_i + r_o)/2)$, from $(T_i + T_o)/2$. These differences along with the corresponding deviations in ϑ_{mid} become more pronounced at smaller η. This effect has also been observed in previous studies (Gastine *et al.* 2015; Fu *et al.* 2024). From figure 1(*a*), it can be seen clearly that the bulk temperature increases with increasing Pr. For example, at $Ra = 10^7$, $\eta = 0.2$, $Pr = 0.1$, the temperature drop across the outer thermal boundary layer is 9.7 % of the total temperature drop across the shell. On the other hand, at $\eta = 0.2$, $Pr = 50$, the temperature drop across the outer thermal boundary layer becomes 16.2 % of the total temperature drop. As Pr is varied over two and a half orders of magnitude, the temperature drop across the outer thermal boundary layer varies by approximately 67 %.

The asymmetry is also present in the time and horizontally averaged radial velocity profile $Re(r)$. As shown in figure 1(*b*), two peaks are observed in the radial velocity profile. The peak value near the inner boundary is higher than that near the outer boundary, indicating greater turbulence intensity in the vicinity of the inner boundary. At fixed Ra and Pr, the difference between the inner and outer peak values is higher at smaller η, which is again due to the larger differences in curvature and gravity between the inner and outer boundaries at smaller η. It is also observed that Re is higher at lower Pr for fixed Ra and

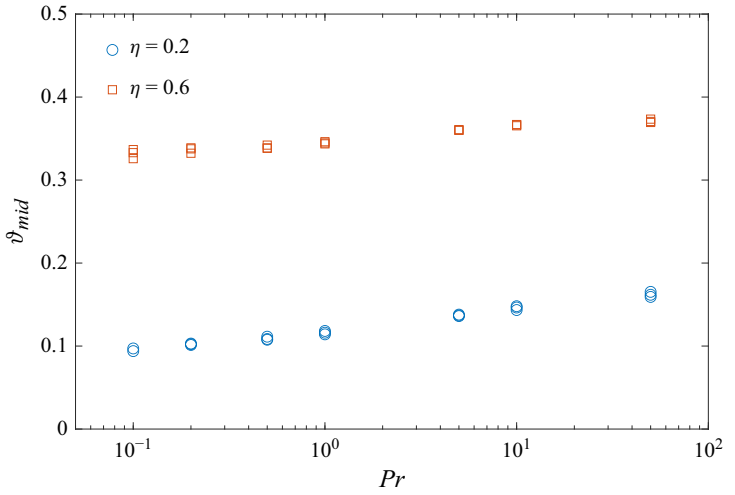

Figure 2. Bulk temperature $\vartheta_{mid} = \vartheta((r_i + r_o)/2)$ with respect to Pr at different η, for $Ra \geqslant 5 \times 10^6$.

η. This occurs as the viscous effects are less significant compared to the thermal diffusion at lower Pr.

The asymmetry can also be quantified by the ratios of the inner and outer thermal and viscous boundary layer thicknesses. These are denoted as $\lambda^i_\vartheta/\lambda^o_\vartheta$ and λ^i_u/λ^o_u, where λ_ϑ and λ_u represent the thermal and viscous boundary layer thicknesses, respectively. The superscripts i and o refer to the boundary layer thicknesses calculated at the inner and outer boundaries, respectively. We define the thermal and viscous boundary layer thicknesses using the slope method (Shishkina *et al.* 2010; Gastine *et al.* 2015). The thermal boundary layer thickness is defined as the distance where the linear fit of $\vartheta(r)$ at the boundary intersects the horizontal line $r = r_{mid}$. The time and horizontally averaged radial profile of the horizontal velocity, $Re_h(r)$, is used to characterise the viscous boundary layer. The viscous boundary layer is defined as the region between the boundary and the point where the linear fit of $Re_h(r)$ near the boundary intersects the horizontal line drawn from the local peak of the curve.

Since the temperature drop is chiefly concentrated near the boundaries, it is reasonable to assume that the entire temperature drop occurs within the thermal boundary layers, leading to

$$\Delta\vartheta_i + \Delta\vartheta_o = 1 \tag{3.1}$$

and

$$\Delta\vartheta_i = 1 - \vartheta_{mid}, \quad \Delta\vartheta_o = \vartheta_{mid}. \tag{3.2}$$

Figure 2 shows ϑ_{mid} as a function of Pr at $\eta = 0.2, 0.6$ for $Ra \geqslant 5 \times 10^6$. As discussed earlier in this section, ϑ_{mid} increases with increasing Pr. For the case $\eta = 0.2$, as Pr increases, ϑ_{mid} rises from 0.097 at $Pr = 0.1$ to 0.162 at $Pr = 50$, with absolute difference 0.065, corresponding to an approximately 67 % increase. On the other hand, for $\eta = 0.6$, ϑ_{mid} changes from 0.326 at $Pr = 0.1$ to 0.373 at $Pr = 50$, resulting in absolute difference 0.047, which corresponds to an increase of approximately 14.4 %. This illustrates that Pr dependence of ϑ_{mid} changes with η. This result aligns with our expectations, as when $\eta \to 1$, $\vartheta_{mid} \to 0.5$, leading to a reduced Pr dependence of ϑ_{mid}.

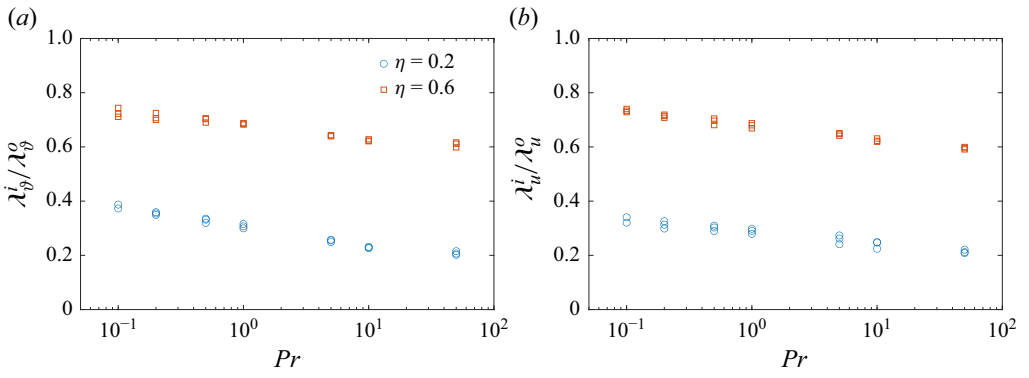

Figure 3. Ratio of the inner and the outer (*a*) thermal boundary layer thickness $\lambda^i_\vartheta/\lambda^o_\vartheta$, and (*b*) viscous boundary layer thickness λ^i_u/λ^o_u, at different η and Pr for $Ra \geqslant 5 \times 10^6$.

The boundary layer thickness ratios $\lambda^i_\vartheta/\lambda^o_\vartheta$ and λ^i_u/λ^o_u are shown in figure 3. As mentioned above, the chosen Rayleigh numbers are $Ra \geqslant 5 \times 10^6$. At the same Pr and η, the values of λ^i_u/λ^o_u are almost identical to those of $\lambda^i_\vartheta/\lambda^o_\vartheta$. As shown in the figure, both $\lambda^i_\vartheta/\lambda^o_\vartheta$ and λ^i_u/λ^o_u decrease with increasing Pr, indicating that the asymmetry in boundary layer thicknesses becomes more pronounced at higher Pr. As an example, $\lambda^i_\vartheta/\lambda^o_\vartheta$ decreases from 0.387 at $Pr = 0.1$ to 0.207 at $Pr = 50$ for $\eta = 0.2$, with absolute difference 0.18 and relative change 86.9 %. In the case $\eta = 0.6$, $\lambda^i_\vartheta/\lambda^o_\vartheta$ decreases from 0.722 at $Pr = 0.1$ to 0.612 at $Pr = 50$, with absolute difference 0.11 and relative change 15.2 %. The differences in $\lambda^i_\vartheta/\lambda^o_\vartheta$ and λ^i_u/λ^o_u with respect to Pr are smaller for $\eta = 0.6$ compared to $\eta = 0.2$. This indicates a weaker Pr dependence of the boundary layer thickness ratios at higher η. This behaviour is expected, as $\eta \to 1$, $\lambda^i_\vartheta/\lambda^o_\vartheta \to 1$ and $\lambda^i_u/\lambda^o_u \to 1$, indicating weaker Pr dependence in the $\eta \to 1$ limit.

4. Evaluation of models

In the following sections, we focus on the thermal boundary layer asymmetry, characterised by $\Delta\vartheta_i$, $\Delta\vartheta_o$ and $\lambda^i_\vartheta/\lambda^o_\vartheta$, as the primary metrics.

In order to determine the three unknowns $\Delta\vartheta_i$, $\Delta\vartheta_o$ and $\lambda^i_\vartheta/\lambda^o_\vartheta$, (3.1)–(3.2) can be utilised. However, an additional relation is still required. Several assumptions have been proposed to derive the third relation. For instance, Gastine *et al.* (2015) derive the third relation based on the assumption of equivalence of the mean plume density within the inner and outer thermal boundary layers. This assumption was validated in their simulations at $Pr = 1$. Similarly, Wu & Libchaber (1991), in their experimental study on non-Boussinesq effects with low-temperature helium gas, found that the two thermal boundary layers adjust their temperature drops and thicknesses such that their thermal fluctuations are equal. This finding was later confirmed by Zhang, Childress & Libchaber (1997) in a follow-up experimental study using glycerol. Therefore, the equivalence of thermal fluctuation scales can also provide the third relation. Puthenveettil & Arakeri (2005) derived expressions for the heat flux through the thermal boundary layers based on the laminar natural convection boundary layer model of Rotem & Claassen (1969). By applying the principle of the conservation of heat flux, the third relation can be obtained by matching the heat fluxes at the inner and outer thermal boundary layers. In a two-dimensional cylindrical geometry with an infinite Pr, Jarvis (1993) proposed that the inner and outer thermal boundary layers are equally stable, resulting in equal thermal

boundary layer Rayleigh numbers at both the surfaces. In a follow-up study, Vangelov & Jarvis (1994) applied this assumption to a two-dimensional asymmetric spherical model to obtain the third relation. This assumption was shown to work well in characterising the thermal boundary layer asymmetry in their simulations with an infinite Pr.

However, none of these assumptions has been validated across different Pr regimes. The range of applicability of the aforementioned assumptions remains unclear. In this section, we will examine the validity of these assumptions at different Pr.

4.1. *Inter-plume density equivalence model*

Proposed by Gastine *et al.* (2015), the inter-plume density equivalence model assumes that the characteristic plume density is equivalent at the edges of both thermal boundary layers. They estimate the characteristic plume separation based on the peak values of the probability distribution function (PDF) of the inter-plume areas at the edges of thermal boundary layers. The characteristic inter-plume density is defined as the number of plumes per unit surface area. Statistics were analysed at a fixed Pr of unity, with different radius ratios and gravity profiles. Their findings indicate that the characteristic inter-plume area is identical at the edges of the inner and outer thermal boundary layers, suggesting that the characteristic plume density is conserved across these surfaces. For the expressions of the characteristic inter-plume distance at the inner and outer surfaces, they use the relations developed by Puthenveettil *et al.* (2011) based on the laminar natural convection boundary layer model of Rotem & Claassen (1969). This approach leads to (Gastine *et al.* 2015)

$$\rho_p^i = \rho_p^o \quad \rightarrow \quad \frac{\alpha g_i \, \Delta\vartheta_i \, (\lambda_\vartheta^i)^5}{\nu\kappa} = \frac{\alpha g_o \, \Delta\vartheta_o \, (\lambda_\vartheta^o)^5}{\nu\kappa}, \tag{4.1}$$

where ρ_p^i, ρ_p^o are plume densities at the edges of the inner and outer thermal boundary layers. Combining (3.1)–(3.2) and (4.1), together with $g_i/g_o = (r_o/r_i)^2 = 1/\eta^2$, we obtain the relations (Gastine *et al.* 2015)

$$\Delta\vartheta_i = \frac{1}{1+\eta^{4/3}}, \quad \Delta\vartheta_o = \vartheta_{mid} = \frac{\eta^{4/3}}{1+\eta^{4/3}}, \quad \frac{\lambda_\vartheta^i}{\lambda_\vartheta^o} = \eta^{2/3}. \tag{4.2}$$

These relations quantify the thermal boundary layer asymmetry derived from this model. The validation of this model will be discussed in § 4.5. The assumption on which this model rests, namely the equivalency of the characteristic plume density at the two boundaries, will also be examined carefully in § 5.

4.2. *Thermal fluctuation equivalence model*

The thermal fluctuation equivalence model was initially proposed by Castaing *et al.* (1989). They divided the flow domain into three regions: the boundary layers adjacent to the boundary, the mixing zone where plumes detach from the boundary layer and accelerate towards the bulk, and the turbulent bulk. Based on their theoretical arguments, the characteristic temperature fluctuation scale in the mixing zone, ϑ^{mix}, was derived. They further assumed that ϑ^{mix} is equivalent to the characteristic temperature fluctuation scale in the turbulent bulk, ϑ^{bulk}, resulting in the relation

$$\vartheta^{bulk} = \vartheta^{mix} = \frac{\kappa\nu}{\alpha g \lambda_\vartheta^3}, \tag{4.3}$$

where symbols have their usual meanings. For the first time, Wu & Libchaber (1991) applied and successfully validated this relation in their studies of non-Boussinesq convection in helium. Zhang *et al.* (1997) later confirmed the validity of this assumption in

the experiments using glycerol. Gastine *et al.* (2015) applied this assumption to determine the boundary layer temperature drop in spherical RBC with different gravity profiles ($g \sim r$, 1, $1/r^2$, $1/r^5$) and $0.2 \leqslant \eta \leqslant 0.95$, at $Pr = 1$. It was observed that this assumption held true only when $g \sim 1/r^2$. Wang *et al.* (2022) applied this assumption in axially co-rotating centrifugal convection system with cold inner and hot outer cylinders. The temperature drop and boundary layer thickness ratio derived from this assumption showed good agreement with their DNS data. In this study, we investigate the range of Pr for which this assumption is applicable in spherical RBC with $g \sim 1/r^2$.

Invoking (4.3) at both the inner and outer thermal boundary layers yields

$$\vartheta^i = \vartheta^{bulk} = \vartheta^o \quad \rightarrow \quad \frac{\kappa\nu}{\alpha g_i (\lambda_\vartheta^i)^3} = \frac{\kappa\nu}{\alpha g_o (\lambda_\vartheta^o)^3}. \tag{4.4}$$

Combining (4.4) with (3.1)–(3.2) leads to the same relations as those given by (4.2), with $g_i/g_o = 1/\eta^2$.

4.3. *Inter-plume distance Ra equivalence model*

Using the similarity solutions for a laminar natural-convection boundary layer in the limit $Pr \rightarrow \infty$ (Rotem & Claassen 1969), Puthenveettil & Arakeri (2005) derived the following expression for Nu at the boundaries:

$$Nu = -\frac{5 \times 2^{-14/15}}{3} Ra_l^{-2/15} Ra^{1/3} C(Pr), \tag{4.5}$$

where $Ra_l = \alpha g \, \Delta\vartheta_w \, l^3/(\nu\kappa)$ is the Rayleigh number based on the mean inter-plume distance near the thermal boundary layer, and $\Delta\vartheta_w$ is the temperature drop across the thermal boundary layer. Note that (4.5) applies only for large values of Pr. The coefficient $C(Pr)$ is a function of Pr but remains nearly constant when $Pr > 5$ (Rotem & Claassen 1969; Puthenveettil & Arakeri 2005), with asymptotic value $C(Pr \rightarrow \infty) = -0.4601$.

The conservation of Nu at the inner and outer boundaries yields

$$Nu_i = Nu_o \quad \Longrightarrow \quad Ra_l^i = Ra_l^o \quad \Longrightarrow \quad \frac{\alpha g_i \, \Delta\vartheta_i \, \bar{l}_i^3}{\nu\kappa} = \frac{\alpha g_o \, \Delta\vartheta_o \, \bar{l}_o^3}{\nu\kappa}, \tag{4.6}$$

where

$$\bar{l}_i \sim \sqrt{\frac{\alpha g_i \, \Delta\vartheta_i \, (\lambda_\vartheta^i)^5}{\nu\kappa}}, \quad \bar{l}_o \sim \sqrt{\frac{\alpha g_o \, \Delta\vartheta_o \, (\lambda_\vartheta^o)^5}{\nu\kappa}} \tag{4.7}$$

represent the mean inter-plume distances at the inner and outer thermal boundary layers (Puthenveettil *et al.* 2011).

By combining (3.1)–(3.2) with (4.6)–(4.7), we obtain the relations

$$\Delta\vartheta_i = \frac{1}{1+\eta}, \quad \Delta\vartheta_o = \vartheta_{mid} = \frac{\eta}{1+\eta}, \quad \frac{\lambda_\vartheta^i}{\lambda_\vartheta^o} = \eta. \tag{4.8}$$

Equation (4.8) describes the asymmetry of the thermal boundary layer.

4.4. *Boundary layer Ra equivalence model*

In the mantle convection with an infinite Pr, it is hypothesised that the temperature field adjusts so that the local thermal boundary layer Rayleigh numbers are equal at both boundaries. The thermal boundary layer Rayleigh numbers are defined by using the thermal boundary layer thickness as the length scale, and the thermal boundary layer

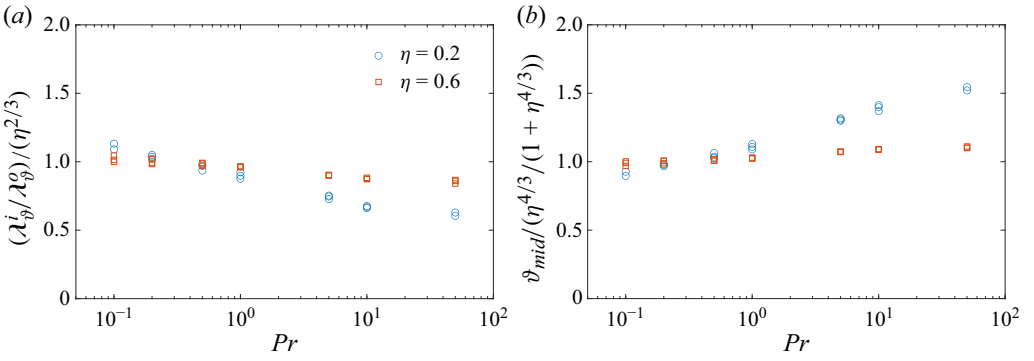

Figure 4. (*a*) Compensated plot of $\lambda^i_\vartheta/\lambda^o_\vartheta$ and (*b*) compensated plot of ϑ_{mid}, based on (4.2).

temperature drop as the temperature scale. This assumption implies that neither boundary layer is more unstable than the other, leading to the relation

$$Ra^i_{\lambda_\vartheta} = Ra^o_{\lambda_\vartheta} \quad \rightarrow \quad \frac{\alpha g_i\, \Delta\vartheta_i\, (\lambda^i_\vartheta)^3}{\nu\kappa} = \frac{\alpha g_o\, \Delta\vartheta_o\, (\lambda^o_\vartheta)^3}{\nu\kappa}. \tag{4.9}$$

Jarvis (1993) first applied this assumption in a two-dimensional, cylindrical shell model of mantle convection with uniform gravity. He derived the thermal boundary layer asymmetry and found a good agreement with his data. Vangelov & Jarvis (1994) further applied this assumption in an axisymmetric spherical model of mantle convection, achieving satisfactory results. Combining (3.1)–(3.2) and (4.9) for a spherical shell with $g \sim 1/r^2$, we recover (4.8), implying that the assumptions in this subsection and § 4.3 lead to identical results for thermal boundary layer asymmetry.

The validation range (with respect to Pr) of all the models presented above will be discussed in the next subsection.

4.5. *Model validation*

In this study, we examine four widely used assumptions in spherical RBC to quantify the asymmetry of the thermal boundary layers. These four assumptions lead to two different relations as presented in (4.2) and (4.8). These relations can be expressed generally as

$$\frac{\lambda^i_\vartheta}{\lambda^o_\vartheta} = \eta^\gamma, \quad \Delta\vartheta_i = \frac{1}{1+\eta^{(2-\gamma)}}, \quad \Delta\vartheta_o = \vartheta_{mid} = \frac{\eta^{(2-\gamma)}}{1+\eta^{(2-\gamma)}}, \tag{4.10}$$

where $\gamma = \gamma_1 = 2/3$ for the inter-plume density equivalence and thermal fluctuation equivalence models, and $\gamma = \gamma_2 = 1$ for the inter-plume distance Ra equivalence and boundary layer Ra equivalence models.

Figure 4 shows the compensated plots of $\lambda^i_\vartheta/\lambda^o_\vartheta$ and ϑ_{mid}, as calculated using (4.2), with respect to Pr. It is observed that the thermal boundary layer asymmetry relations derived from the inter-plume density equivalence model and the thermal fluctuation equivalence model show good agreement with the DNS data within the range $0.2 \lesssim Pr \lesssim 1$. The deviation becomes increasingly significant outside this range. As we will demonstrate later, in § 5, this breakdown arises because the fundamental assumption underlying the model – the equivalence of the characteristic inter-plume distance at the inner and outer boundaries – no longer holds outside this Pr regime. Gastine *et al.* (2015) similarly reported that the inter-plume density equivalence model performs well at $Pr = 1$. In § 5, we further evaluate

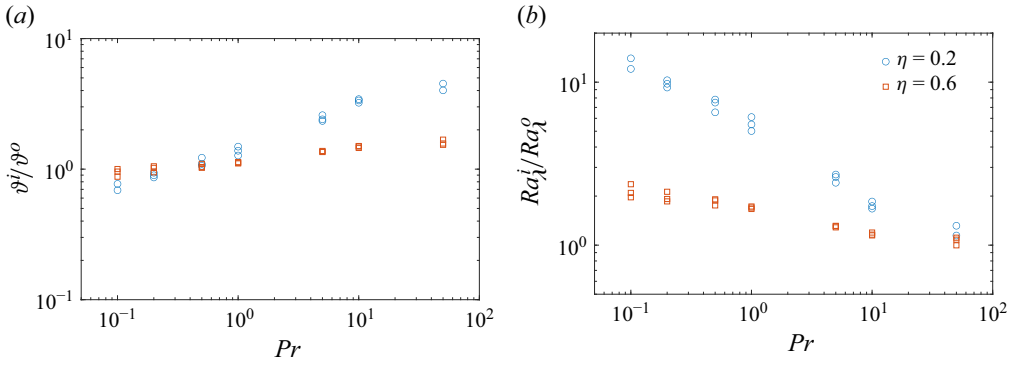

Figure 5. Ratios of the inner and outer (*a*) temperature fluctuation scales, ϑ^i/ϑ^o, based on (4.4), and (*b*) boundary layer Rayleigh numbers, $Ra^i_{\lambda_\vartheta}/Ra^o_{\lambda_\vartheta}$, based on (4.9).

this underlying assumption across a range of Pr, and demonstrate that it does not hold for $1 < Pr \leqslant 50$ and $Pr = 0.1$.

Figure 5(*a*) shows ϑ^i/ϑ^o as a function of Pr. The results indicate that the inner and outer thermal fluctuation scales are nearly equivalent for $0.2 \lesssim Pr \lesssim 1$, but exhibit increasing deviations outside this range. Overall, $0.2 \lesssim Pr \lesssim 1$ is identified as a suitable validation range for both the inter-plume density equivalence model and the thermal fluctuation equivalency model. The reason why the thermal fluctuation equivalence model fails outside this Pr regime can be understood by examining the plume dynamics and boundary layer structures. For very low Pr (e.g. $Pr = 0.1$), thermal diffusivity dominates, causing the plumes to broaden significantly. This makes the boundary layers more susceptible to the large-scale disturbances, and thus disrupts the symmetry of the thermal fluctuation scales. At very high Pr (e.g. $Pr = 50$), viscosity dominates and suppresses heat transport, leading to thinner plumes and reduced thermal fluctuations. Consequently, the equivalence between the thermal fluctuation scales of the inner and outer boundary layers no longer holds. This mechanism is consistent with previous findings on boundary layer asymmetry caused by extreme variations in fluid properties and plume dynamics (Castaing *et al.* 1989; Wu & Libchaber 1991; Zhang *et al.* 1997), and explains why the assumption underlying the thermal fluctuation equivalence model ceases to be valid outside the intermediate Pr number range.

Figure 6 presents the compensated plot of thermal boundary layer asymmetry using (4.8). It is evident that within the range of Pr considered, the relations derived from the inter-plume distance Ra equivalence model and the boundary layer Ra equivalence model show good agreement with the DNS data only at the high Pr value of 50.

The reason why these models are valid exclusively in the high-Pr regime can be understood through the plume and boundary layer dynamics inherent to high-viscosity fluids. According to Puthenveettil & Arakeri (2005), (4.5) was derived under the assumption that viscous effects dominate, a condition typically satisfied at large Pr. At large Pr, viscosity stabilises the boundary layers, resulting in thinner and more well-defined plume structures. This ensures that the plume separation distance, or equivalently, the thermal boundary layer thickness, is determined primarily by boundary layer instabilities. Thus the core assumption $Ra^i_{\lambda_\vartheta} = Ra^o_{\lambda_\vartheta}$ underlying these models holds robustly at high Pr, as illustrated directly in figure 5(*b*).

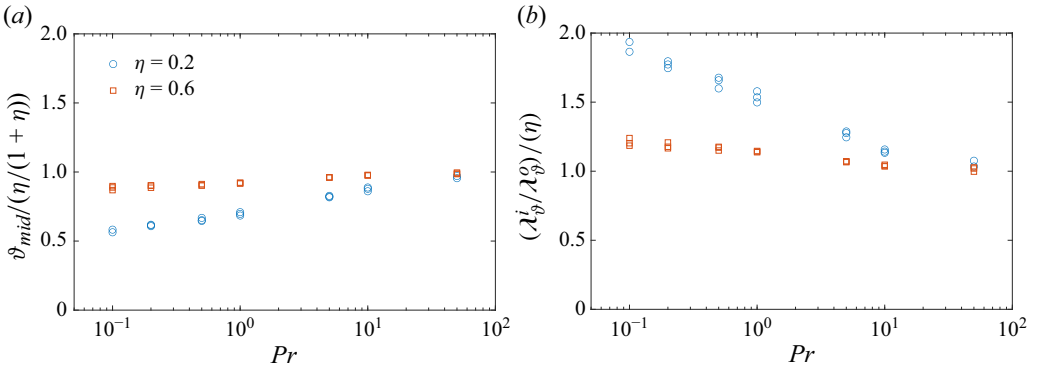

Figure 6. Compensated plot of (*a*) ϑ_{mid} and (*b*) $\lambda^i_\vartheta/\lambda^o_\vartheta$, based on (4.8).

Moreover, the inter-plume distance Ra equivalence model was originally formulated for mantle convection scenarios where $Pr \to \infty$ (Jarvis 1993; Vangelov & Jarvis 1994), further highlighting the fundamental dependence of the model assumptions on extremely viscous regimes. Our simulations clearly demonstrate that the equivalence of boundary layer Rayleigh numbers is fulfilled only at $Pr = 50$, confirming that both the inter-plume distance Ra equivalence model and the boundary layer Ra equivalence model are inherently applicable solely in high-Pr environments.

5. Characteristic inter-plume distance

In the models discussed in § 4, two among them rely on estimating the characteristic inter-plume distance. The inter-plume density equivalence model assumes that the characteristic inter-plume distance is identical at both the inner and outer boundaries, while the inter-plume distance Ra equivalence model assumes the equivalency of Ra_l at the boundaries. Accurate estimation of the characteristic inter-plume distance is therefore essential. In this section, the method for estimating the characteristic inter-plume distance will be discussed. Additionally, the dependence of the inter-plume distance on Pr will also be analysed. We also examine the basic assumptions underlying both the inter-plume density equivalence model and the inter-plume distance Ra equivalence model. Finally, for $Pr = 0.1$ and 50, we propose and validate two new models based on the characteristic inter-plume distance.

5.1. *Inter-plume distance estimation*

To estimate the characteristic plume distance, we first need to delineate and extract the thermal plume from the surrounding turbulent background. Various methods exist for defining a thermal plume. For example, Zhou & Xia (2002) used the local temperature fluctuations T' to define a thermal plume. On the other hand, Shishkina & Wagner (2006, 2008) applied the local thermal dissipation rate as a criterion for thermal plume extraction. Additionally, vertical velocity has also been used for this purpose (Julien *et al.* 1999). Vipin & Puthenveettil (2013) found that the divergence of the horizontal velocity field could also effectively identify thermal plumes, as regions with negative divergence coincide with the areas of positive vertical acceleration in fluid parcels – a key feature of hot plumes. Gastine *et al.* (2015) compared the plume structures detected by the aforementioned methods, and reported that using the temperature fluctuations yields relatively better results in terms of the shape of the plume contours. We adopt the criterion

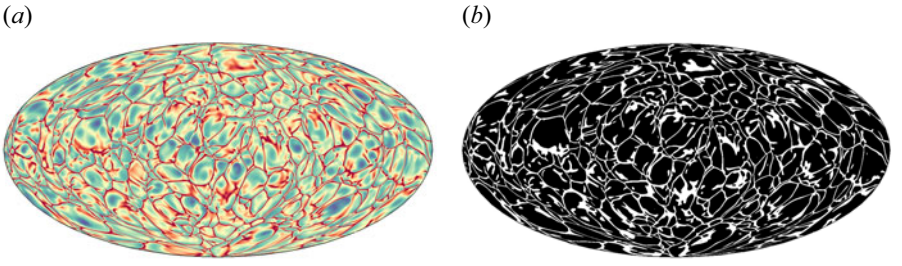

Figure 7. (*a*) Temperature fluctuation (T') contours at the edge of the inner thermal boundary layer ($r = r_i + 0.0138$) for $Pr = 50$, $\eta = 0.6$, $Ra = 5 \times 10^7$. The colour scale ranges from $T' = -0.2$ (dark blue) to $T' = 0.2$ (dark red). (*b*) Binarised version of (*a*), following (5.1). The white regions represent plumes, and the black regions represent inter-plume islands.

used by Gastine *et al.* (2015). Specifically, the plumes are defined as

$$\begin{cases} T - \overline{\langle T \rangle_s} \geqslant \frac{1}{2}\sigma_{sd} & \text{at } r = r_i + \lambda_\vartheta^i, \\ T - \overline{\langle T \rangle_s} \leqslant -\frac{1}{2}\sigma_{sd} & \text{at } r = r_o - \lambda_\vartheta^o, \end{cases} \tag{5.1}$$

where σ_{sd} is the time and horizontally averaged standard deviation of temperature, defined as

$$\sigma_{sd}(r) = \overline{\sqrt{\left\langle \left(T - \overline{\langle T \rangle_s}\right)^2 \right\rangle_s}}. \tag{5.2}$$

Figure 7(*a*) shows the instantaneous temperature field at the edge of the inner thermal boundary layer, with the red regions representing the up-rising hot plumes, and the blue regions indicating the cold inter-plume regions. The plumes connect to form sheet-like structures (Shishkina & Wagner 2008; Stevens *et al.* 2018). Following (5.1), figure 7(*a*) is binarised, and the results are shown in figure 7(*b*). The white regions represent hot plumes, while the black regions represent inter-plume regions. The sheet-like plumes isolate the inter-plume areas into separate 'islands'.

Puthenveettil & Arakeri (2005) and Zhou & Xia (2010) demonstrated that the statistics of the thermal plumes in turbulent RBC follow a log-normal distribution. Gastine *et al.* (2015) investigated the statistics of the areas of the inter-plume islands in spherical RBC, and observed a similar distribution. They used the mean plume distances ($\bar{l}_i, \bar{l}_o$) derived from the convective boundary layer model (4.7) to estimate the mean plume separation, and further related it to the characteristic inter-plume areas ($\overline{A}_i, \overline{A}_o$) as

$$\overline{A}_i \sim \frac{\pi}{4}\bar{l}_i^2, \quad \overline{A}_o \sim \frac{\pi}{4}\bar{l}_o^2, \tag{5.3}$$

where the subscripts i and o have their usual meanings. They further used the area corresponding to the peak of the PDF of the inter-plume areas to estimate the characteristic inter-plume area from their simulations. Additionally, they observed that $\pi\bar{l}_i^2/4$, $\pi\bar{l}_o^2/4$ closely align with the peak values of the PDFs in their simulations, concluding that (5.3) provides a reliable estimate of the characteristic inter-plume area.

The area of an inter-plume island, $A(r)$, at radial position $r = r_o$ is calculated by

$$A(r = r_o) = r_o^2 \iint_\Sigma \sin\theta \, \mathrm{d}\theta \, \mathrm{d}\phi, \tag{5.4}$$

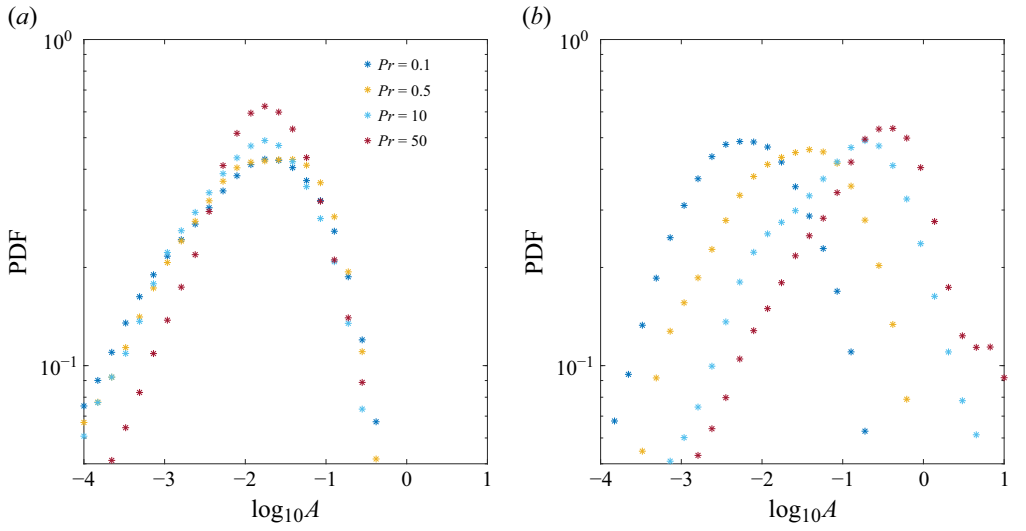

Figure 8. The PDFs of the inter-plume area for (*a*) the inner thermal boundary layer, and (*b*) the outer thermal boundary layer, at $\eta = 0.2,\ Ra = 10^7$.

where Σ represents the boundary of the inter-plume island, and θ and ϕ are the co-latitude and longitude, respectively. We identify all inter-plume islands located at the radial positions $r = r_i + \lambda_\vartheta^i$ and $r = r_o - \lambda_\vartheta^o$, and calculate the area of each island using (5.4). The PDFs of the inter-plume areas are averaged over a total time interval of at least 100 convective time units. The resulting PDFs are consistent with those of Gastine *et al.* (2015).

In the present work, we define the area corresponding to the peak of the PDF as the characteristic inter-plume area. Using $\mathcal{A}_i$ and $\mathcal{A}_o$, the characteristic inter-plume areas at the edges of the inner and outer thermal boundary layers, we define characteristic inter-plume distances L_i and L_o as

$$\mathcal{A}_i = \frac{\pi}{4} L_i^2, \quad \mathcal{A}_o = \frac{\pi}{4} L_o^2. \tag{5.5}$$

Gastine *et al.* (2015) demonstrated that the characteristic inter-plume areas are equivalent at the inner and outer thermal boundary layers at $Pr = 1$. They developed a model to quantify thermal boundary layer asymmetry based on this observation, as introduced in § 4.1. However, as already discussed, we observe significant deviations from this assumption when Pr is not unity. In the next subsection, we examine how the inter-plume area varies with Pr.

5.2. *Inter-plume area: Pr dependence*

In this subsection, we explore the Pr dependence of the characteristic inter-plume areas at the inner and outer thermal boundary layers.

Figure 8 presents the time-averaged PDFs of the inter-plume areas for both thermal boundary layers at $\eta = 0.2,\ Ra = 10^7$ across different Pr values. As shown in figure 8(*a*), the characteristic inter-plume area for the inner thermal boundary layer remains unchanged for $0.1 \leqslant Pr \leqslant 50$. In contrast, the characteristic inter-plume area for the outer thermal boundary layer increases with Pr. This difference highlights that the Pr dependence of the characteristic inter-plume area varies between the inner and outer boundary layers.

Figure 9 provides qualitative insight into this phenomenon. The instantaneous contour plots of the binarised temperature fluctuations near the inner and outer boundary layers at

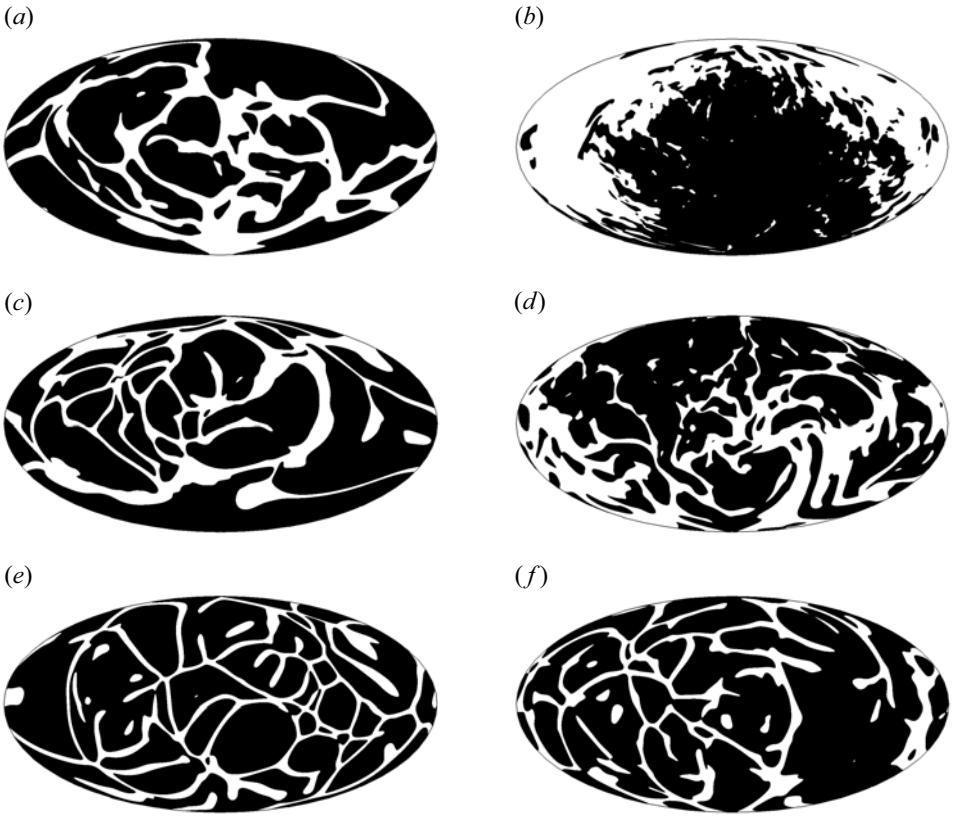

Figure 9. Contour plots of the binarised temperature fluctuations for (*a*,*c*,*e*) the inner thermal boundary layer, and (*b*,*d*,*f*) the outer thermal boundary layer, at $\eta = 0.2$, $Ra = 10^7$, for (*a*,*b*) $Pr = 0.1$, (*c*,*d*) $Pr = 1$, (*e*,*f*) $Pr = 50$.

$\eta = 0.2$ for different Pr are shown. The morphology and distribution of inter-plume islands change significantly with increasing Pr; they become more fragmented at both boundary layers. However, this fragmentation is more pronounced near the outer boundary layer. For example, at $Pr = 0.1$, a 'super-island' exists near the outer boundary layer, where the thermal plumes (white regions in the binarised plot) are thick, leaving the inter-plume areas scattered and small. As Pr increases, smaller islands emerge and the plumes become thinner, leading to a larger number of inter-plume islands. The plumes become thinner also at the inner boundary layer with increasing Pr, but the characteristic inter-plume area remains constant. Moreover, the distribution of inter-plume islands becomes increasingly similar between the inner and outer thermal boundary layers as Pr increases.

Figure 10 shows the time-averaged PDFs of the inter-plume areas near the inner and outer thermal boundary layers for $\eta = 0.6$, $Ra = 10^7$ at different Pr. The PDFs for both the inner and outer thermal boundary layers exhibit a similar trend in their Pr dependence, with the characteristic inter-plume area increasing as Pr increases. However, while the Pr dependence of the characteristic inter-plume area is comparable between the two boundary layers, the increase is more pronounced near the outer thermal boundary layer than near the inner one. As Pr increases, the thermal plumes become thinner, resulting in a larger characteristic inter-plume area. At $Pr = 50$, the morphology and the distribution of the

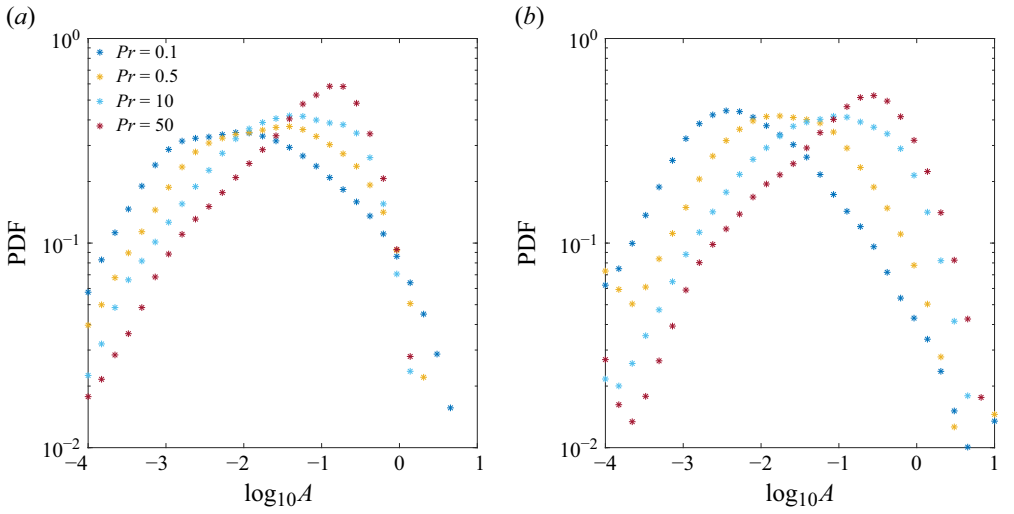

Figure 10. The PDFs of the inter-plume area for (*a*) the inner thermal boundary layer, and (*b*) the outer thermal boundary layer, at $\eta = 0.6$, $Ra = 10^7$.

inter-plume islands become notably similar between the inner and outer thermal boundary layers, as shown in figure 11.

The Pr dependence of the inter-plume area also helps to explain our earlier observation in § 3 that the asymmetry exhibits a weaker dependence on Pr at higher values of η. Qualitatively, as η approaches unity, the boundary layers become increasingly symmetric, significantly reducing asymmetries induced by variations in Pr. Furthermore, plume morphology and the statistical analysis of characteristic inter-plume areas also support this understanding. Specifically, at smaller radius ratios (e.g. $\eta = 0.2$), radial differences in curvature and gravity ($g \sim 1/r^2$) between the inner and outer boundaries are pronounced, causing significant variations in plume dynamics as Pr changes. In contrast, at higher radius ratios (e.g. $\eta = 0.6$), these radial differences diminish, resulting in more symmetric boundary layer conditions and consequently a weaker sensitivity of the asymmetry to changes in Pr.

We now examine the basic assumption of the inter-plume density equivalence model, which posits that the characteristic plume separations are identical near the inner and outer thermal boundary layers. In Gastine *et al.* (2015), this equivalence of characteristic plume separation was reformulated as the equivalence of characteristic inter-plume area. Based on the PDF of the inter-plume areas, they demonstrated that the characteristic inter-plume area is nearly identical near the inner and outer thermal boundary layers for $Pr = 1$. Following their methodology, we estimate the variation in characteristic plume separation by analysing the variation in the characteristic inter-plume area.

Figure 12 presents the time-averaged PDFs of the inter-plume area near the inner and outer thermal boundary layers for $\eta = 0.2$, $Ra = 10^7$ at various Pr. As shown in the figure, the characteristic inter-plume area for the outer thermal boundary layer is smaller than that for the inner boundary layer at $Pr = 0.1$. Moreover, the characteristic inter-plume area for the outer thermal boundary layer increases with Pr, whereas it remains unchanged for the inner boundary layer, as previously illustrated in figure 8. The characteristic inter-plume area for the outer thermal boundary layer surpasses that of the inner boundary layer at approximately $Pr = 0.5$, and becomes significantly larger for $Pr \geqslant 5$.

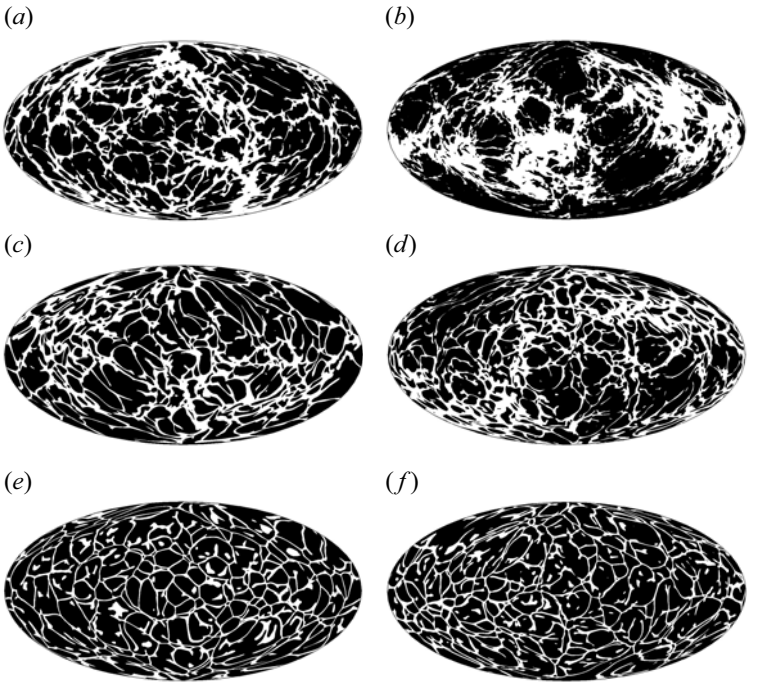

Figure 11. Contour plots of the binarised temperature fluctuations for (*a*,*c*,*e*) the inner thermal boundary layer, and (*b*,*d*,*f*) the outer thermal boundary layer, at $\eta = 0.6$, $Ra = 10^7$, for (*a*,*b*) $Pr = 0.1$, (*c*,*d*) $Pr = 1$, (*e*,*f*) $Pr = 50$.

Figure 13 shows the corresponding PDFs for $\eta = 0.6$, $Ra = 10^7$. Similar to the $\eta = 0.2$ case, the characteristic inter-plume area for the outer thermal boundary layer is initially smaller than that for the inner boundary layer, at $Pr = 0.1$. It surpasses the characteristic inter-plume area of the inner boundary layer at approximately $Pr = 5$ (though this specific case is not explicitly shown in figure 13). Furthermore, as the asymmetry decreases with increasing η, PDFs for the inner and outer thermal boundary layers are similar at $\eta = 0.6$ in comparison to the PDFs at $\eta = 0.2$.

From the above discussion, it follows that the characteristic inter-plume areas near the inner and outer boundary layers are not equal for either $Pr = 0.1$ or $5 \leqslant Pr \leqslant 50$. Consequently, $0.2 \lesssim Pr \lesssim 1$ is identified as the appropriate validation range for the basic assumption of the inter-plume density equivalence model, which is in line with the range determined by comparing the thermal boundary layer asymmetry derived from this model, as discussed in § 4.5.

5.3. *Proposed model for small Pr*

As demonstrated in the previous subsection, the PDFs of the inter-plume areas exhibit a dependence on Pr. At $Pr = 0.1$, the characteristic inter-plume area near the inner thermal boundary layer ($\mathcal{A}_i$) is larger than that near the outer thermal boundary layer ($\mathcal{A}_o$). By analysing the PDFs of the inter-plume areas near both boundaries, we identify the following relation between $\mathcal{A}_i$ and $\mathcal{A}_o$:

$$\mathcal{A}_i \lambda_\vartheta^i = \mathcal{A}_o \lambda_\vartheta^o, \tag{5.6}$$

where λ_ϑ^i and λ_ϑ^o represent the thicknesses of the inner and outer thermal boundary layers, respectively.

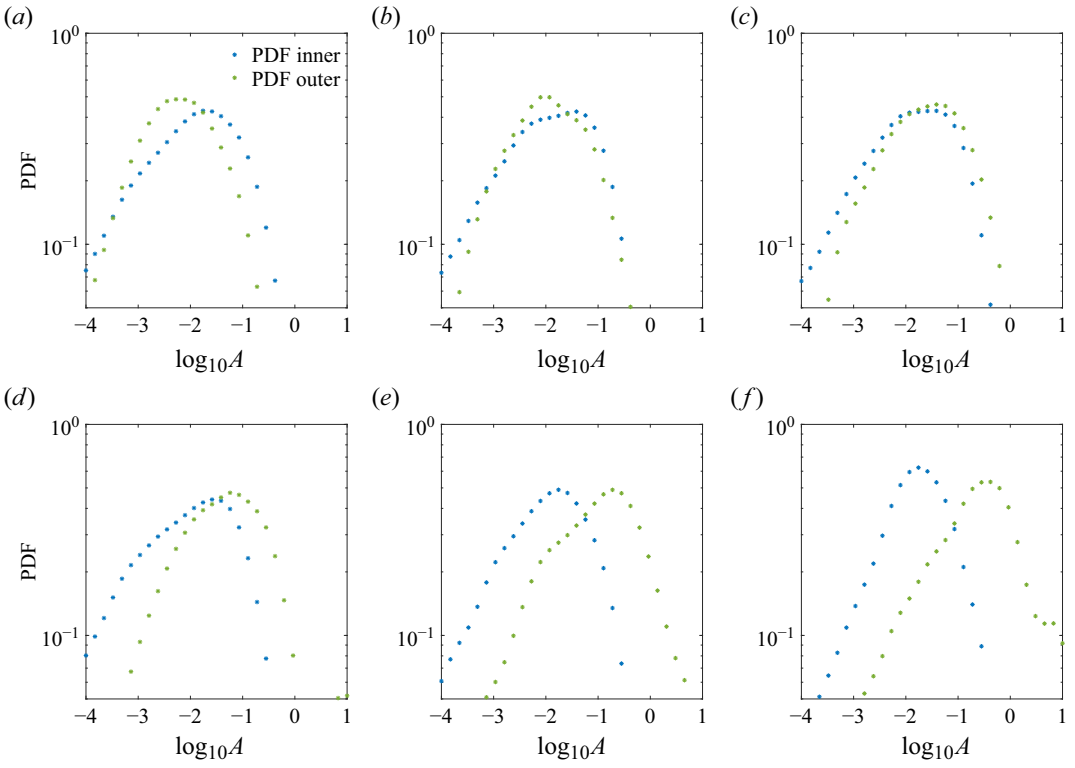

Figure 12. Time-averaged PDFs of the inter-plume areas for the inner (blue) and outer (green) thermal boundary layers at $\eta = 0.2$, $Ra = 10^7$, at different Pr values: (*a*) $Pr = 0.1$, (*b*) $Pr = 0.2$, (*c*) $Pr = 0.5$, (*d*) $Pr = 1$, (*e*) $Pr = 10$, (*f*) $Pr = 50$.

This model can be regarded as an extension of the inter-plume density equivalence model, which is based on the assumption that the characteristic inter-plume areas are identical near the inner and outer boundaries. This assumption can be interpreted as stating that the average surface area occupied by a single plume is the same at both boundaries. However, we find that this assumption does not hold at $Pr = 0.1$. Instead, (5.6) holds, which can be interpreted as the average volume occupied by a plume being equal between the two boundaries. This revised assumption shares a similar physical picture with the original inter-plume density equivalence model, but is better suited to describing the flow characteristics near $Pr = 0.1$.

Figures 14 and 15 display the time-averaged PDFs of the inter-plume areas on a logarithmic scale ($\log_{10} A$) and the PDFs of the inter-plume area multiplied by the corresponding thermal boundary layer thickness ($\log_{10}(\lambda_\vartheta A)$). As shown in figures 14(*b*) and 15(*b*), the peak values of the PDFs for the inner and outer thermal boundary layers align, validating (5.6), as both λ_ϑ^i and λ_ϑ^o are constant.

Using the mean plume density defined in (4.7) to estimate the characteristic inter-plume area, we have

$$\mathcal{A}_i \approx \frac{\pi}{4}\bar{l}_i^2, \quad \mathcal{A}_o \approx \frac{\pi}{4}\bar{l}_o^2. \tag{5.7}$$

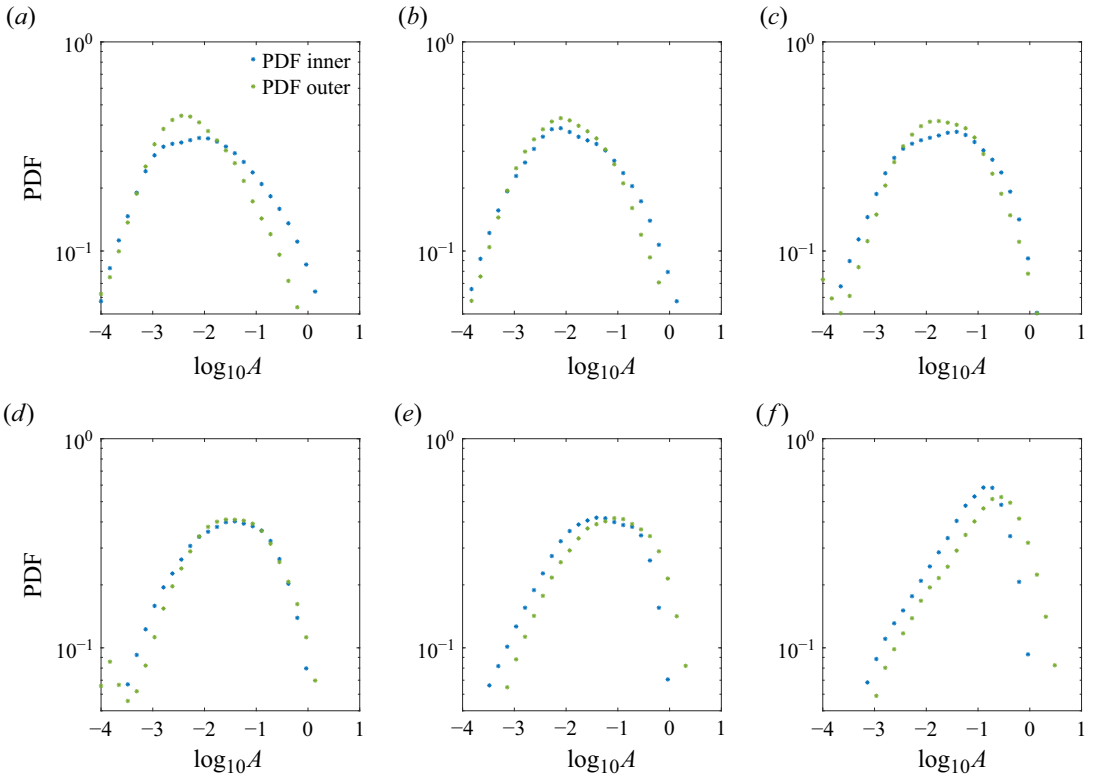

Figure 13. Time-averaged PDFs of the inter-plume areas for the inner (blue) and outer (green) thermal boundary layers at $\eta = 0.6$, $Ra = 10^7$, at different Pr values: (*a*) $Pr = 0.1$, (*b*) $Pr = 0.2$, (*c*) $Pr = 0.5$, (*d*) $Pr = 1$, (*e*) $Pr = 10$, (*f*) $Pr = 50$.

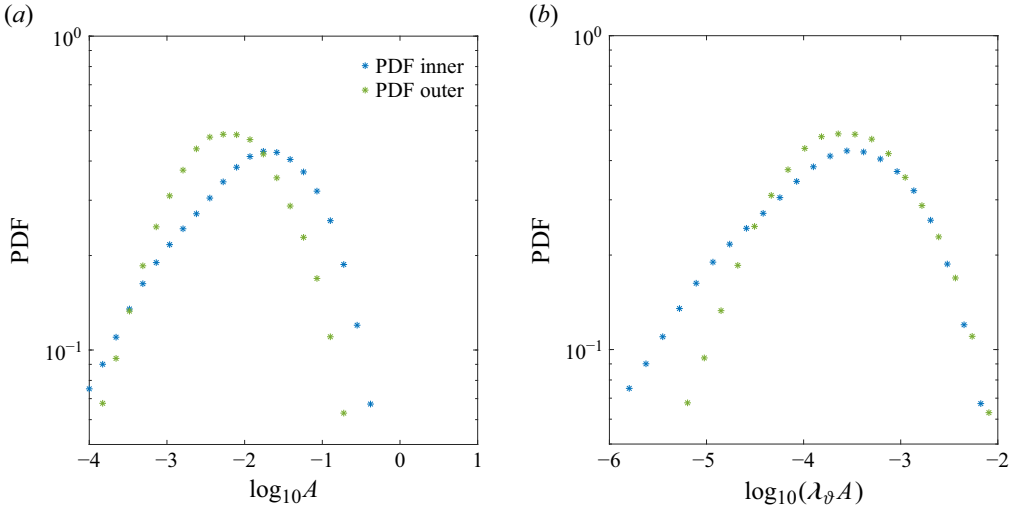

Figure 14. Time-averaged PDFs of the inter-plume areas for the inner (blue) and outer (green) thermal boundary layers at $\eta = 0.2$, $Ra = 10^7$: (*a*) original PDF and (*b*) scaled PDF. In (*b*), the blue symbols represent the scaled PDF of $\lambda_\vartheta^i A_i$, and the green symbols denote the scaled PDF of $\lambda_\vartheta^o A_o$.

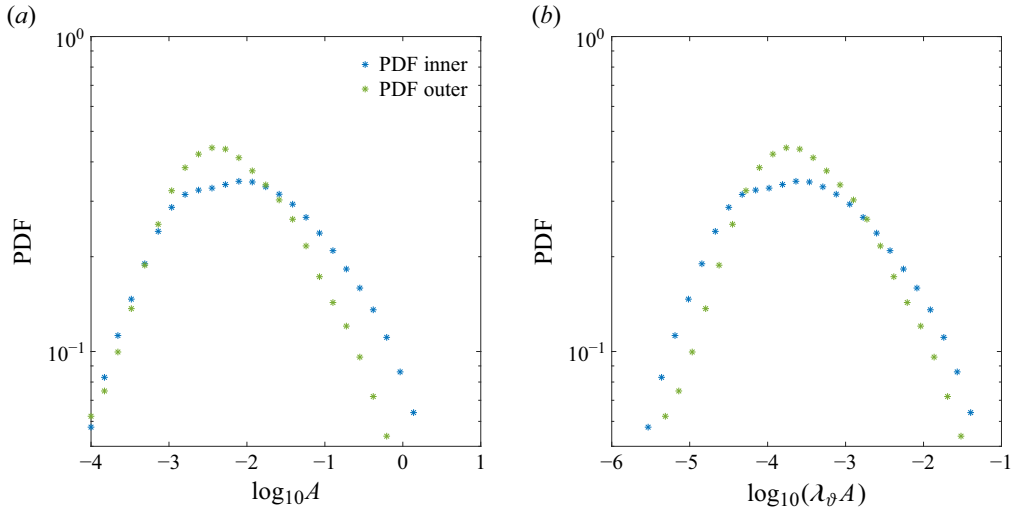

Figure 15. Time-averaged PDFs of the inter-plume areas for the inner (blue) and outer (green) thermal boundary layers at $\eta = 0.6$, $Ra = 10^7$: (*a*) original PDF and (*b*) scaled PDF. In (*b*), the blue symbols represent the scaled PDF of $\lambda_\vartheta^i A_i$, and the green symbols denote the scaled PDF of $\lambda_\vartheta^o A_o$.

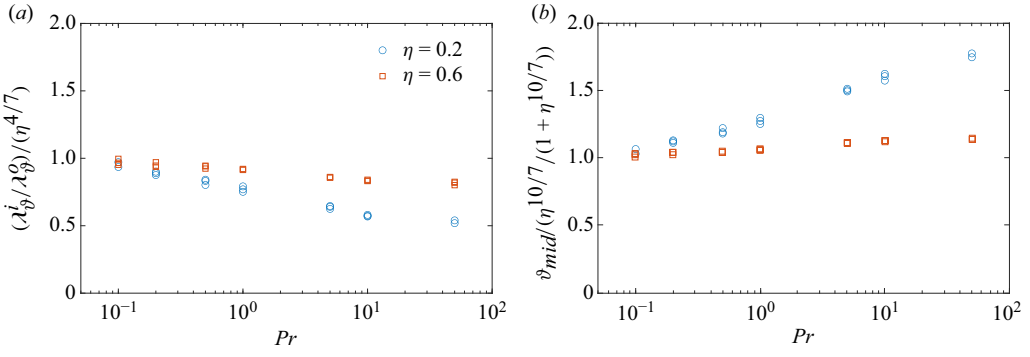

Figure 16. Compensated plot of (*a*) $\lambda_\vartheta^i/\lambda_\vartheta^o$, and (*b*) ϑ_{mid}, based on (5.9).

Substituting this into (5.6) gives

$$\bar{l}_i^2 \lambda_\vartheta^i = \bar{l}_o^2 \lambda_\vartheta^o \quad \Rightarrow \quad \frac{\alpha g_i \, \Delta\vartheta_i \, (\lambda_\vartheta^i)^6}{\nu\kappa} = \frac{\alpha g_o \, \Delta\vartheta_o \, (\lambda_\vartheta^o)^6}{\nu\kappa}, \tag{5.8}$$

which provides a new relation for deriving the thermal boundary layer asymmetry. Combining this with (3.1) and (3.2) yields

$$\Delta\vartheta_i = \frac{1}{1+\eta^{10/7}}, \quad \Delta\vartheta_o = \vartheta_{mid} = \frac{\eta^{10/7}}{1+\eta^{10/7}}, \quad \frac{\lambda_\vartheta^i}{\lambda_\vartheta^o} = \eta^{4/7}. \tag{5.9}$$

Figure 16 demonstrates the validity of (5.9) at the smallest Prandtl number ($Pr = 0.1$) considered in our simulations. The results presented in figure 16 demonstrate excellent agreement with the scaling relation given by (5.9) for both $\eta = 0.2$ and $\eta = 0.6$. Given that our model shares a similar physical picture with the inter-plume density equivalence model, and considering that the latter has already been validated over a broad range of η values in the studies by Gastine *et al.* (2015) and Fu *et al.* (2024), we anticipate that our

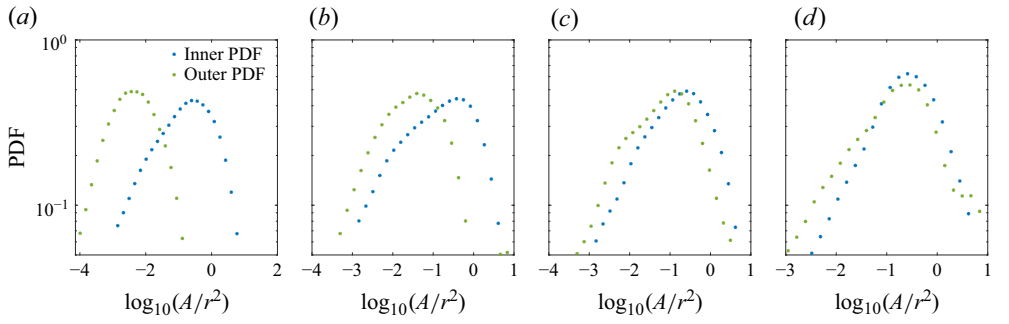

Figure 17. The PDFs of the normalised inter-plume areas from (5.10) at $Ra = 10^7$, $\eta = 0.2$, for (*a*) $Pr = 0.1$, (*b*) $Pr = 1$, (*c*) $Pr = 10$, (*d*) $Pr = 50$.

proposed model can be reasonably extrapolated to other η values as well. Furthermore, our model is consistent in the limit $\eta \to 1$, as it correctly predicts symmetric boundary layer temperature drops ($\vartheta_{mid} = 1/2$) and equal boundary layer thicknesses ($\lambda^i_\vartheta / \lambda^o_\vartheta = 1$), thus reinforcing its robustness and physical reliability.

5.4. *Proposed model for large Pr*

In § 5.2, we demonstrated that the morphology and distribution of inter-plume areas become increasingly similar between the inner and outer thermal boundary layers as Pr increases. For instance, at $Pr = 50$, $\eta = 0.6$, the morphologies of inter-plume islands near the inner and outer thermal boundary layers appear quite similar, as shown in figures 11(*e*,*f*). However, despite the similar appearance of the Hammer projections at high Pr, the physical scales remain different. The total surface area of the edge of the inner thermal boundary layer is approximately $(r_i/r_o)^2$ times smaller than that of the outer thermal boundary layer. Motivated by this observation, we propose a new assumption for the large Pr regime. To begin, we define the normalised inter-plume area $\tilde{A}(r)$ at a radial location $r = r_o$ as

$$\tilde{A}(r = r_o) = \frac{A(r = r_o)}{r_o^2} = \iint_{\Sigma} \sin\theta \mathrm{d}\theta \mathrm{d}\phi, \tag{5.10}$$

where Σ represents the boundary of an inter-plume island. We compute the PDF of the normalised inter-plume area, and define the characteristic normalised inter-plume area $\tilde{\mathcal{A}}$ as the value corresponding to the peak value of this PDF.

Our assumption is that as Pr increases, the characteristic normalised inter-plume areas near the inner and outer thermal boundary layers converge and eventually become identical at sufficiently large Pr. This is from the observation that the inter-plume islands become increasingly similar in shape at the inner and outer boundaries, which then, upon normalising with the surface area ($4\pi r^2$) term, gives equivalent PDF peaks. Figures 17 and 18 display the PDFs of the normalised inter-plume areas at $Ra = 10^7$ for various Pr values, with $\eta = 0.2$ and $\eta = 0.6$, respectively. It is evident that the characteristic normalised inter-plume areas near the inner and outer thermal boundary layers approach each other as Pr increases, and become nearly identical at $Pr = 50$.

Based on the above finding, we establish the following relation at $Pr = 50$:

$$\tilde{\mathcal{A}}_i = \tilde{\mathcal{A}}_o \quad \Rightarrow \quad \frac{\mathcal{A}_i}{r_i^2} = \frac{\mathcal{A}_o}{r_o^2}. \tag{5.11}$$

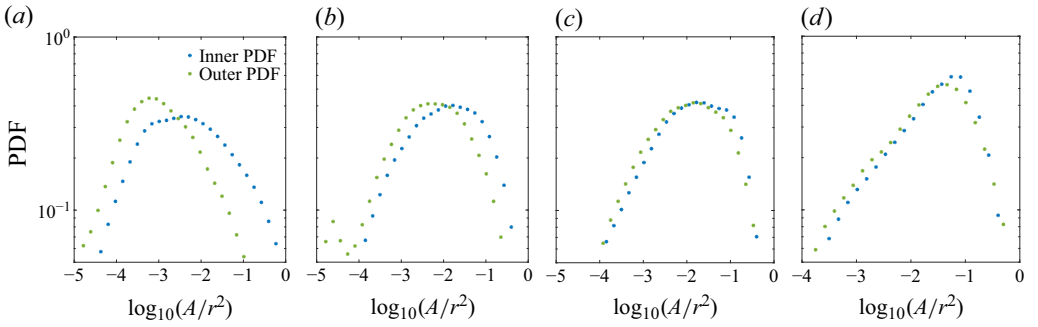

Figure 18. The PDFs of the normalised inter-plume areas from (5.10) at $Ra = 10^7$, $\eta = 0.6$, for (*a*) $Pr = 0.1$, (*b*) $Pr = 1$, (*c*) $Pr = 10$, (*d*) $Pr = 50$.

Model	Assumption	γ	Validation range
Proposed model for small Pr (§ 5.3)	$\mathcal{A}_i \lambda_\vartheta^i = \mathcal{A}_o \lambda_\vartheta^o$	$\frac{4}{7}$	$Pr = 0.1$
Inter-plume density equivalence model (§ 4.1)	$\rho_p^i = \rho_p^o$	$\frac{2}{3}$	$0.2 \lesssim Pr \lesssim 1$
Thermal fluctuation equivalence model (§ 4.2)	$\vartheta^i = \vartheta^o$	$\frac{2}{3}$	$0.2 \lesssim Pr \lesssim 1$
Inter-plume distance Ra equivalence model (§ 4.3)	$Ra_l^i = Ra_l^o$	1	$Pr = 50$
Boundary layer Ra equivalence model (§ 4.4)	$Ra_{\lambda_\vartheta}^i = Ra_{\lambda_\vartheta}^o$	1	$Pr = 50$
Proposed model for large Pr (§ 5.4)	$\mathcal{A}_i / \mathcal{A}_o = \eta^2$	1	$Pr = 50$

Table 2. Comparison of thermal boundary layer asymmetry models analysed in this study. The parameter γ represents the exponent in the thermal boundary layer asymmetry equation (4.10).

Substituting (4.7) and (5.7) into (5.11), we can write

$$\frac{\mathcal{A}_i}{\mathcal{A}_o} = \frac{\bar{l}_i^2}{\bar{l}_o^2} = \eta^2 \quad \Rightarrow \quad \frac{\alpha g_i \, \Delta\vartheta_i \, (\lambda_\vartheta^i)^5}{\nu\kappa} = \frac{\alpha g_o \, \Delta\vartheta_o \, (\lambda_\vartheta^o)^5}{\nu\kappa} \eta^2. \tag{5.12}$$

Equation (5.12) serves as the third relation for describing thermal boundary layer asymmetry. Combining this equation with (3.1) and (3.2) leads to the same results as in (4.8). As discussed in § 4.5, (4.8) provides an accurate description at $Pr = 50$. Furthermore, our model for the high-Pr regime also remains consistent in the limiting case as $\eta \to 1$. In this planar limit, the temperature drops across the inner and outer boundary layers become symmetric, satisfying $\vartheta_{mid} = 1/2$, and the boundary layer thickness ratio approaches unity, i.e. $\lambda_\vartheta^i / \lambda_\vartheta^o = 1$. These conditions align precisely with the expected symmetry and known results from planar RBC. Thus this consistency further supports the robustness and physical validity of our proposed high-Pr model.

The details of all thermal boundary layer asymmetry models examined in this study are summarised in table 2. Additionally, the assumptions underlying each model and their respective validation ranges in Pr space are also listed.

6. Conclusion and outlook

In this study, we investigated the thermal boundary layer asymmetry of turbulent Rayleigh–Bénard convection (RBC) in spherical shells across a range of Prandtl numbers ($0.1 \leqslant Pr \leqslant 50$) and radius ratios ($\eta = 0.2, 0.6$) using direct numerical simulations (DNS). A centrally condensed mass with gravity profile $g(r) = (r_o/r)^2$ was considered. Two key parameters were employed to quantify the asymmetry of the thermal boundary layers: the time and horizontally averaged bulk temperature ϑ_{mid}, and the thermal boundary layer thickness ratio $\lambda^i_\vartheta/\lambda^o_\vartheta$. The dependence of these parameters on η was investigated for different Pr regimes.

We analysed four widely used thermal boundary layer asymmetry models using our DNS data, and examined their underlying assumptions. It was found that the *inter-plume density equivalence model* and the *thermal fluctuation equivalence model* are valid for $0.2 \lesssim Pr \lesssim 1$, whereas the *inter-plume distance Ra equivalence model* and the *boundary layer Ra equivalence model* are valid only at $Pr = 50$. These findings demonstrate that each model has a distinct validation range in Pr space.

We examined the Pr dependence of the PDF of the inter-plume area. The Pr dependence of the characteristic inter-plume area differed between the two boundaries. For $\eta = 0.2$, the characteristic inter-plume area increased with Pr for the outer thermal boundary layer, while it remained unchanged for the inner thermal boundary layer within the entire range $0.1 \leqslant Pr \leqslant 50$. For $\eta = 0.6$, the characteristic inter-plume area increased for both boundary layers, but the increase was more pronounced for the outer boundary layer. At $Pr = 0.1$, the characteristic inter-plume area was larger for the inner boundary layer than the outer one, but this trend reversed for $5 \leqslant Pr \leqslant 50$.

By analysing our simulation data, we found that the relation $\mathcal{A}_i \lambda^i_\vartheta = \mathcal{A}_o \lambda^o_\vartheta$ holds at $Pr = 0.1$. Based on this relation, a new model for the thermal boundary layer asymmetry at $Pr = 0.1$ was proposed and validated against DNS data. Furthermore, we observed that the morphologies of inter-plume areas become increasingly similar as Pr increases. Building upon this observation, we proposed that $\mathcal{A}_i/\mathcal{A}_o = \eta^2$ holds for large values of Pr. This relation was validated at $Pr = 50$. The proposed model yielded results consistent with the *inter-plume density equivalence model* and the *boundary layer Ra equivalence model*, and showed excellent agreement with DNS data at $Pr = 50$.

It is important to emphasise that all our analyses and conclusions are obtained specifically for the centrally condensed mass with the gravity profile $g(r) \sim 1/r^2$, which is representative of convection within spherical shells characteristic of planetary atmospheres, such as gas giants. The applicability of our results to other gravity profiles, such as the linear profile $g(r) \sim r$ relevant to terrestrial mantle convection, is not straightforward. Indeed, different gravity distributions will alter buoyancy forcing and boundary layer instabilities significantly, particularly at low Pr where thermal diffusivity dominates the plume dynamics. Thus further targeted studies are necessary to quantitatively evaluate the robustness of our proposed scaling relations under alternative gravity conditions.

Moreover, an important aspect for future research is to examine the validity and robustness of the proposed models under more extreme parameter regimes. Specifically, extending our models to significantly higher Rayleigh numbers would be valuable, as the current scaling relationships are based on local balances and statistical properties verified primarily within the range $5 \times 10^6 \leqslant Ra \leqslant 5 \times 10^7$. While our results demonstrate consistency across the considered Ra range, some deviations might arise at much higher Ra, potentially due to transitions to different turbulent regimes. Additionally, investigating the applicability of our models at smaller radius ratios ($\eta \ll 1$) remains an open

https://doi.org/10.1017/jfm.2025.10497 Published online by Cambridge University Press

Ra	Nu	$Err(Nu)$	Re	ϑ_{mid}	$\lambda^i_\vartheta/\lambda^o_\vartheta$	λ^i_u/λ^o_u	$\epsilon^{bulk}_\vartheta$	ϵ^{bulk}_u	$N^i_{\lambda_\vartheta}/N^o_{\lambda_\vartheta}$	$N^i_{\lambda_u}/N^o_{\lambda_u}$	$N_r \times l_{max}$
					$Pr=0.1, \quad \eta=0.2$						
5×10^6	9.11	1.03 %	2899.93	0.0939	(0.0199 / 0.0514)	(0.0048 / 0.0141)	0.3077	0.8377	(30 / 47)	(15 / 25)	321×597
1×10^7	11.31	1.17 %	3952.90	0.0971	(0.0160 / 0.0429)	(0.0037 / 0.0115)	0.3071	0.8303	(34 / 54)	(17 / 28)	401×650
					$Pr=0.1, \quad \eta=0.6$						
5×10^6	11.24	0.32 %	2847.51	0.3258	(0.0360 / 0.0484)	(0.0091 / 0.0123)	0.2818	0.8747	(40 / 46)	(21 / 24)	321×768
1×10^7	13.67	1.12 %	3830.76	0.3330	(0.0293 / 0.0406)	(0.0075 / 0.0103)	0.2941	0.8445	(45 / 52)	(23 / 26)	401×853
5×10^7	21.88	1.35 %	7881.36	0.3367	(0.0182 / 0.0256)	(0.0044 / 0.0060)	0.3085	0.8372	(45 / 53)	(23 / 26)	513×1536
					$Pr=0.2, \quad \eta=0.2$						
5×10^6	9.98	0.72 %	1786.54	0.1013	(0.0181 / 0.0504)	(0.0059 / 0.0181)	0.2990	0.8447	(22 / 36)	(13 / 22)	241×512
1×10^7	12.46	0.72 %	2495.39	0.1023	(0.0145 / 0.0409)	(0.0047 / 0.0150)	0.3030	0.8492	(26 / 43)	(15 / 27)	321×597
5×10^7	20.40	1.23 %	5432.10	0.1030	(0.0088 / 0.0252)	(0.0029 / 0.0097)	0.3197	0.7961	(25 / 42)	(15 / 27)	401×960
					$Pr=0.2, \quad \eta=0.6$						
5×10^6	12.39	0.07 %	1783.63	0.3323	(0.0324 / 0.0447)	(0.0110 / 0.0153)	0.2765	0.8629	(29 / 34)	(18 / 20)	241×682
1×10^7	15.18	0.31 %	2447.02	0.3376	(0.0262 / 0.0371)	(0.0092 / 0.0130)	0.2827	0.8772	(35 / 41)	(21 / 25)	321×768
5×10^7	24.27	0.98 %	5089.32	0.3388	(0.0163 / 0.0233)	(0.0060 / 0.0084)	0.3060	0.8674	(34 / 41)	(21 / 25)	401×1066
					$Pr=0.5, \quad \eta=0.2$						
5×10^6	10.98	0.54 %	933.14	0.1076	(0.0164 / 0.0489)	(0.0078 / 0.0252)	0.2998	0.8263	(11 / 19)	(8 / 14)	121×341
1×10^7	13.59	0.72 %	1329.12	0.1085	(0.0132 / 0.0398)	(0.0065 / 0.0213)	0.2989	0.8273	(13 / 22)	(10 / 16)	161×426
5×10^7	22.54	0.92 %	2844.33	0.1113	(0.0079 / 0.0247)	(0.0040 / 0.0138)	0.2932	0.8397	(20 / 34)	(14 / 25)	321×597
					$Pr=0.5, \quad \eta=0.6$						
5×10^6	13.47	0.18 %	951.63	0.3382	(0.0295 / 0.0418)	(0.0148 / 0.0210)	0.2594	0.8253	(15 / 17)	(11 / 13)	121×426
1×10^7	16.48	0.26 %	1312.05	0.3388	(0.0241 / 0.0343)	(0.0124 / 0.0178)	0.2813	0.8439	(17 / 20)	(13 / 15)	161×512
5×10^7	26.50	0.36 %	2764.76	0.3421	(0.0149 / 0.0216)	(0.0081 / 0.0119)	0.2908	0.8715	(26 / 32)	(20 / 24)	321×768
					$Pr=1, \quad \eta=0.2$						
5×10^6	11.65	0.62 %	557.20	0.1141	(0.0155 / 0.0491)	(0.0093 / 0.0312)	0.2899	0.8303	(9 / 15)	(7 / 12)	97×256
1×10^7	14.36	0.72 %	764.01	0.1161	(0.0124 / 0.0404)	(0.0076 / 0.0263)	0.2872	0.8396	(10 / 17)	(8 / 14)	121×256
5×10^7	23.93	0.91 %	1701.59	0.1182	(0.0074 / 0.0247)	(0.0050 / 0.0179)	0.3089	0.8381	(12 / 22)	(11 / 19)	201×426

Table 3. For caption see next page.

https://doi.org/10.1017/jfm.2025.10497 Published online by Cambridge University Press

Ra	Nu	$Err(Nu)$	Re	ϑ_{mid}	$\lambda^i_\vartheta/\lambda^o_\vartheta$	λ^i_u/λ^o_u	$\epsilon^{bulk}_\vartheta$	ϵ^{bulk}_u	$N^i_{\lambda_\vartheta}/N^o_{\lambda_\vartheta}$	$N^i_{\lambda_u}/N^o_{\lambda_u}$	$N_r \times l_{max}$
					$Pr=1, \quad \eta=0.6$						
5×10^6	13.96	0.24 %	564.78	0.3436	(0.0282 / 0.0410)	(0.0178 / 0.0259)	0.2516	0.8159	(12 / 14)	(10 / 11)	97×288
1×10^7	17.05	0.48 %	789.17	0.3447	(0.0231 / 0.0337)	(0.0155 / 0.0228)	0.2569	0.8194	(13 / 16)	(11 / 13)	121×426
5×10^7	27.31	0.96 %	1698.69	0.3462	(0.0144 / 0.0211)	(0.0105 / 0.0157)	0.2762	0.8376	(14 / 16)	(12 / 14)	161×512
					$Pr=5, \quad \eta=0.2$						
5×10^6	12.87	0.17 %	159.80	0.1361	(0.0136 / 0.0528)	(0.0134 / 0.0490)	0.2504	0.7952	(9 / 16)	(9 / 15)	97×256
1×10^7	15.86	0.42 %	230.74	0.1369	(0.0110 / 0.0431)	(0.0113 / 0.0431)	0.2530	0.8132	(10 / 17)	(10 / 17)	121×256
5×10^7	26.06	0.56 %	514.18	0.1379	(0.0066 / 0.0265)	(0.0074 / 0.0307)	0.2736	0.8498	(12 / 22)	(12 / 24)	201×426
					$Pr=5, \quad \eta=0.6$						
5×10^6	14.54	0.23 %	150.31	0.3601	(0.0265 / 0.0412)	(0.0248 / 0.0381)	0.2641	0.7982	(11 / 14)	(11 / 14)	97×288
1×10^7	17.65	0.27 %	214.46	0.3608	(0.0218 / 0.0341)	(0.0221 / 0.0341)	0.2371	0.8066	(11 / 13)	(11 / 13)	97×288
5×10^7	27.85	0.19 %	486.07	0.3599	(0.0138 / 0.0215)	(0.0161 / 0.0251)	0.2802	0.8363	(13 / 16)	(14 / 18)	161×512
					$Pr=10, \quad \eta=0.2$						
5×10^6	13.30	0.77 %	89.96	0.1434	(0.0128 / 0.0553)	(0.0146 / 0.0588)	0.2625	0.7906	(16 / 32)	(17 / 33)	201×426
1×10^7	16.40	1.02 %	132.18	0.1464	(0.0103 / 0.0451)	(0.0128 / 0.0517)	0.2679	0.7963	(17 / 34)	(19 / 37)	241×682
5×10^7	26.75	0.63 %	299.02	0.1480	(0.0063 / 0.0278)	(0.0086 / 0.0383)	0.2637	0.8358	(18 / 36)	(20 / 42)	321×597
					$Pr=10, \quad \eta=0.6$						
5×10^6	14.66	0.33 %	81.82	0.3654	(0.0260 / 0.0414)	(0.0279 / 0.0442)	0.2590	0.8023	(11 / 14)	(12 / 14)	97×288
1×10^7	17.84	0.05 %	117.65	0.3665	(0.0213 / 0.0342)	(0.0239 / 0.0384)	0.2450	0.8160	(24 / 30)	(25 / 32)	241×682
5×10^7	27.90	0.17 %	273.93	0.3669	(0.0136 / 0.0219)	(0.0187 / 0.0302)	0.2585	0.8312	(25 / 32)	(29 / 37)	321×682
					$Pr=50, \quad \eta=0.2$						
5×10^6	14.03	0.31 %	19.82	0.1592	(0.0122 / 0.0567)	(0.0193 / 0.0873)	0.2851	0.8071	(8 / 16)	(10 / 20)	97×256
1×10^7	17.28	0.23 %	29.76	0.1618	(0.0097 / 0.0469)	(0.0165 / 0.0791)	0.2658	0.8193	(14 / 29)	(18 / 38)	201×426
5×10^7	27.81	0.19 %	77.03	0.1653	(0.0060 / 0.0297)	(0.0129 / 0.0609)	0.2789	0.8231	(13 / 28)	(19 / 40)	241×512

Table 3. For caption see next page.

https://doi.org/10.1017/jfm.2025.10497 Published online by Cambridge University Press

Ra	Nu	$Err(Nu)$	Re	ϑ_{mid}	$\lambda^i_\vartheta/\lambda^o_\vartheta$	λ^i_u/λ^o_u	$\epsilon^{bulk}_\vartheta$	ϵ^{bulk}_u	$N^i_{\lambda_\vartheta}/N^o_{\lambda_\vartheta}$	$N^i_{\lambda_u}/N^o_{\lambda_u}$	$N_r \times l_{max}$
					$Pr = 50, \quad \eta = 0.6$						
5×10^6	14.95	0.22 %	17.77	0.3694	(0.0254 / 0.0412)	(0.0322 / 0.0537)	0.2511	0.8180	(11 / 14)	(13 / 16)	97×288
1×10^7	18.14	0.12 %	26.10	0.3706	(0.0208 / 0.0340)	(0.0286 / 0.0484)	0.2424	0.8385	(20 / 25)	(23 / 30)	201×597
5×10^7	28.48	0.09 %	65.59	0.3734	(0.0131 / 0.0219)	(0.0246 / 0.0413)	0.2545	0.8411	(19 / 24)	(26 / 33)	241×682

Table 3 (cntd). Simulation details: Ra is the Rayleigh number, Nu is the Nusselt number, $Err(Nu)$ represents the relative error of the four Nusselt numbers, as described in § 2.3, Re denotes the global Reynolds number, ϑ_{mid} is the mean temperature at mid-depth, λ^i_ϑ and λ^o_ϑ are the inner and outer thermal boundary layer thicknesses, respectively, λ^i_u and λ^o_u correspond to the inner and outer viscous boundary layer thicknesses, $\epsilon^{bulk}_\vartheta$ represents the proportion of the bulk contribution to the thermal energy dissipation rate, ϵ^{bulk}_u denotes the proportion of the bulk contribution to the kinetic energy dissipation rate, $N^i_{\lambda_\vartheta}$ and $N^o_{\lambda_\vartheta}$ are the numbers of grid points within the inner and outer thermal boundary layers, respectively, and $N^i_{\lambda_u}$ and $N^o_{\lambda_u}$ represent the numbers of grid points within the inner and outer viscous boundary layers, respectively.

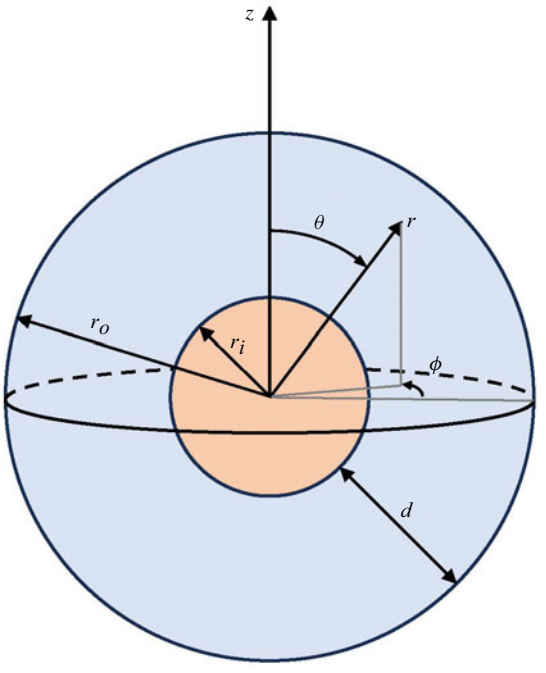

Figure 19. Schematic of the computational domain and coordinate system.

question. Such small-η scenarios introduce increasingly pronounced curvature effects, which may fundamentally alter plume dynamics and boundary layer structures, potentially challenging the underlying assumptions of our models. Exploring these regimes would therefore provide valuable insights into the broader applicability and limitations of our theoretical framework.

Acknowledgements. We thank S. Mukhopadhyay for performing the validations using Dedalus code, and sharing the data with us. We also thank J. Zhong for many helpful discussions.

Funding. We gratefully acknowledge financial support from the Max Planck Society, the German Research Foundation through grants 521319293, 540422505 and 550262949, the Alexander von Humboldt Foundation, the International Max Planck Research School for Solar System Science at the University of Göttingen (IMPRS, Solar System School), and the Daimler Benz Foundation. Part of the simulations have been conducted on the HPC systems of the Max Planck Computing and Data Facility (MPCDF) as well as the National High Performance Computing Centre (NHR@ZIB and NHR-Nord@Göttingen). The authors also gratefully acknowledge the Gauss Centre for Supercomputing e.V. (www.gauss-centre.eu) for funding this project by providing computing time on the GCS Supercomputers SuperMUC-NG at the Leibniz Supercomputing Centre (www.lrz.de) and JUWELS (Jülich Supercomputing Centre 2021) at the Jülich Supercomputing Centre (JSC).

Declaration of interests. The authors report no conflict of interest.

Appendix A. Simulation data and grid resolution

The schematic of the computational domain and the coordinate system is shown in figure 19. The domain is a spherical shell with inner radius r_i and outer radius r_o. We apply no-slip boundary conditions for the velocity at both boundaries. For temperature, we use isothermal boundary conditions: the inner boundary (shown in orange) is kept at a higher temperature T_i, and the outer boundary (shown in blue) at a lower temperature T_o.

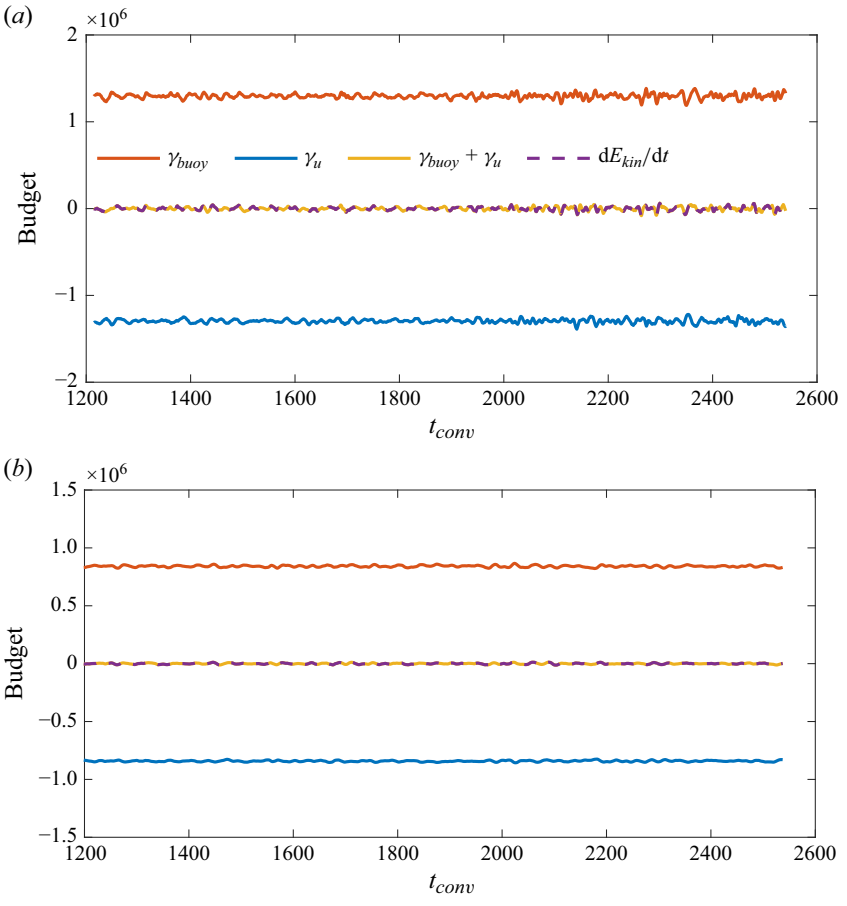

Figure 20. Time series of the volume-averaged buoyancy power $\mathcal{P}_{buoy}$, the volume-averaged kinetic energy dissipation rate ϵ_u, the total energy balance $\mathcal{P}_{buoy} + \epsilon_u$, and the volume-averaged kinetic energy variation rate $\mathrm{d}E_{kin}/\mathrm{d}t$ at (*a*) $\eta = 0.2$, $Ra = 5 \times 10^7$ and (*b*) $\eta = 0.6$, $Ra = 5 \times 10^7$. For both cases, $Pr = 50$.

An appropriate spatial resolution should achieve a balance in the turbulent kinetic energy budget at the statistically steady stage, which is a balance between the volume-averaged buoyancy power input $\mathcal{P}_{buoy}$ and the volume-averaged kinetic energy dissipation rate ϵ_u:

$$\mathcal{P}_{buoy} = \frac{Ra}{Pr} \langle g T u_r \rangle , \quad \epsilon_u = \langle \boldsymbol{u} \cdot \nabla^2 \boldsymbol{u} \rangle. \tag{A1}$$

We present two representative cases in figure 20 at $\eta = 0.2$ and $\eta = 0.6$ for $Ra = 5 \times 10^7$ and $Pr = 50$. The time derivative of the total kinetic energy, $\mathrm{d}E_{kin}/\mathrm{d}t$, is also included in the figure. As is clearly shown, the volume-averaged kinetic energy input from the radial buoyancy flux is well balanced by the volume-averaged viscous dissipation rate in both cases, indicating that the simulations are well resolved. This kinetic energy budget check, combined with the criterion based on the relative differences among four independently computed Nusselt numbers (detailed in § 2.3), constitutes the two primary diagnostics that we use to assess whether a simulation is sufficiently resolved.

References

Ahlers, G., Grossmann, S. & Lohse, D. 2009 Heat transfer and large scale dynamics in turbulent Rayleigh–Bénard convection. *Rev. Mod. Phys.* **81** (2), 503.

Aurnou, J.M., Heimpel, M., Allen, L., King, E. & Wicht, J. 2008 Convective heat transfer and the pattern of thermal emission on the gas giants. *Geophys. J. Intl* **173** (3), 793–801.

Castaing, B., Gunaratne, G., Heslot, F., Kadanoff, L., Libchaber, A., Thomae, S., Wu, X.Z., Zaleski, S. & Zanetti, G. 1989 Scaling of hard thermal turbulence in Rayleigh–Bénard convection. *J. Fluid Mech.* **204**, 1–30.

Chandrasekhar, S. 1981 *Hydrodynamic and Hydromagnetic Stability*. Courier Corporation.

Christensen, U.R. & Aubert, J. 2006 Scaling properties of convection-driven dynamos in rotating spherical shells and application to planetary magnetic fields. *Geophys. J. Intl* **166** (1), 97–114.

Christensen, U.R. & Wicht, J. 2007 Numerical dynamo simulations. *Core Dyn.* **8**, 245–282.

Christensen, U.R. & Wicht, J. 2008 Models of magnetic field generation in partly stable planetary cores: applications to Mercury and Saturn. *Icarus* **196** (1), 16–34.

Davies, G.F. & Richards, M.A. 1992 Mantle convection. *J. Geol.* **100** (2), 151–206.

Deschamps, F., Tackley, P.J. & Nakagawa, T. 2010 Temperature and heat flux scalings for isoviscous thermal convection in spherical geometry. *Geophys. J. Intl* **182** (1), 137–154.

Egbers, C., Beyer, W., Bonhage, A., Hollerbach, R. & Beltrame, P. 2003 The geoflow-experiment on ISS (part I): experimental preparation and design of laboratory testing hardware. *Adv. Space Res.* **32** (2), 171–180.

Fu, Y., Bader, S.H., Song, J. & Zhu, X. 2024 Turbulent spherical Rayleigh–Bénard convection: radius ratio dependence. *J. Fluid Mech.* **1000**, A41.

Futterer, B., Egbers, C., Dahley, N., Koch, S. & Jehring, L. 2010 First identification of sub- and supercritical convection patterns from 'geoflow', the geophysical flow simulation experiment integrated in fluid science laboratory. *Acta Astronaut.* **66** (1–2), 193–200.

Gastine, T., Wicht, J. & Aurnou, J.M. 2015 Turbulent Rayleigh–Bénard convection in spherical shells. *J. Fluid Mech.* **778**, 721–764.

Guillot, T., Stevenson, D.J., Hubbard, W.B. & Saumon, D. 2004 The interior of Jupiter. In *Jupiter: The Planet, Satellites and Magnetosphere* (ed. F. Bagenal, T.E. Dowling & W.B. McKinnon), pp. 35–57. Cambridge University Press.

Hanasoge, S., Gizon, L. & Sreenivasan, K.R. 2016 Seismic sounding of convection in the Sun. *Annu. Rev. Fluid Mech.* **48**, 191–217.

Jarvis, G.T. 1993 Effects of curvature on two-dimensional models of mantle convection: cylindrical polar coordinates. *J. Geophys. Res.: Solid Earth* **98** (B3), 4477–4485.

Jarvis, G.T., Glatzmaierand, G.A. & Vangelov, V.I. 1995 Effects of curvature, aspect ratio and plan form in two- and three-dimensional spherical models of thermal convection. *Geophys. Astrophys. Fluid Dyn.* **79** (1–4), 147–171.

Julien, K., Legg, S., Mcwilliams, J. & Werne, J. 1999 Plumes in rotating convection. Part 1. Ensemble statistics and dynamical balances. *J. Fluid Mech.* **391**, 151–187.

Lago, R., Gastine, T., Dannert, T., Rampp, M. & Wicht, J. 2021 MagIC v5.10: a two-dimensional message-passing interface (MPI) distribution for pseudo-spectral magnetohydrodynamics simulations in spherical geometry. *Geosci. Model Dev.* **14** (12), 7477–7495.

Puthenveettil, B.A. & Arakeri, J.H. 2005 Plume structure in high-Rayleigh-number convection. *J. Fluid Mech.* **542**, 217–249.

Puthenveettil, B.A., Gunasegarane, G.S., Agrawal, Y.K., Schmeling, D., Bosbach, J. & Arakeri, J.H. 2011 Length of near-wall plumes in turbulent convection. *J. Fluid Mech.* **685**, 335–364.

Rotem, Z. & Claassen, L. 1969 Natural convection above unconfined horizontal surfaces. *J. Fluid Mech.* **39** (1), 173–192.

Schubert, G., Turcotte, D.L. & Olson, P. 2001 *Mantle Convection in the Earth and Planets*. Cambridge University Press.

Shah, R.K. & London, A.L. 1978 *Laminar Flow Forced Convection in Ducts: A Source Book for Compact Heat Exchanger Analytical Data*, pp. 477. Academic Press.

Shahnas, M.H., Lowman, J.P., Jarvis, G.T. & Bunge, H.P. 2008 Convection in a spherical shell heated by an isothermal core and internal sources: implications for the thermal state of planetary mantles. *Phys. Earth Planet. Inter.* **168** (1–2), 6–15.

Shishkina, O., Stevens, R.J., Grossmann, S. & Lohse, D. 2010 Boundary layer structure in turbulent thermal convection and its consequences for the required numerical resolution. *New J. Phys.* **12** (7), 075022.

SHISHKINA, O. & WAGNER, C. 2006 Analysis of thermal dissipation rates in turbulent Rayleigh–Bénard convection. *J. Fluid Mech.* **546**, 51–60.

SHISHKINA, O. & WAGNER, C. 2008 Analysis of sheet-like thermal plumes in turbulent Rayleigh–Bénard convection. *J. Fluid Mech.* **599**, 383–404.

STEVENS, R.J., BLASS, A., ZHU, X., VERZICCO, R. & LOHSE, D. 2018 Turbulent thermal superstructures in Rayleigh–Bénard convection. *Phys. Rev. Fluids.* **3** (4), 041501.

TILGNER, A. 1996 High-Rayleigh-number convection in spherical shells. *Phys. Rev. E* **53** (5), 4847.

VANGELOV, V.I. & JARVIS, G.T. 1994 Geometrical effects of curvature in axisymmetric spherical models of mantle convection. *J. Geophys. Res.: Solid Earth* **99** (B5), 9345–9358.

VAZAN, A., HELLED, R., PODOLAK, M. & KOVETZ, A. 2016 The evolution and internal structure of Jupiter and Saturn with compositional gradients. *Astrophys. J.* **829** (2), 118.

VIPIN, K. & PUTHENVEETTIL, B.A. 2013 Identification of coherent structures on the horizontal plate in turbulent convection. In *Proceedings of the 8th World Conference on Experimental Heat Transfer, Fluid Mechanics and Thermodynamics ExHFT*, June 16–20, Lisbon, Portugal.

WANG, D., JIANG, H., LIU, S., ZHU, X. & SUN, C. 2022 Effects of radius ratio on annular centrifugal Rayleigh–Bénard convection. *J. Fluid Mech.* **930**, A19.

WICHT, J. 2002 Inner-core conductivity in numerical dynamo simulations. *Phys. Earth Planet. Inter.* **132** (4), 281–302.

WICHT, J. & SANCHEZ, S. 2019 Advances in geodynamo modelling. *Geophys. Astrophys. Fluid Dyn.* **113** (1–2), 2–50.

WU, X.Z. & LIBCHABER, A. 1991 Non-Boussinesq effects in free thermal convection. *Phys. Rev. A* **43** (6), 2833.

YADAV, R.K., HEIMPEL, M. & BLOXHAM, J. 2020 Deep convection-driven vortex formation on Jupiter and Saturn. *Sci. Adv.* **6** (46), eabb9298.

ZAUSSINGER, F., HAUN, P., SZABO, B., PETER, S., TRAVNIKOV, V., AL KAWWAS, M. & EGBERS, C. 2020 Rotating spherical gap convection in the GeoFlow International Space Station (ISS) experiment. *Phys. Rev. Fluids* **5** (6), 063502.

ZHANG, J., CHILDRESS, S. & LIBCHABER, A. 1997 Non-Boussinesq effect: thermal convection with broken symmetry. *Phys. Fluids* **9** (4), 1034–1042.

ZHOU, Q. & XIA, K. 2010 Physical and geometrical properties of thermal plumes in turbulent Rayleigh–Bénard convection. *New J. Phys.* **12** (7), 075006.

ZHOU, S. & XIA, K. 2002 Plume statistics in thermal turbulence: mixing of an active scalar. *Phys. Rev. Lett.* **89** (18), 184502.